Deepak Singh

Calorimetric Measurement of the Stator Core Losses Caused by Manufacturing

School of Electrical Engineering

Thesis submitted for examination for the degree of Master of Science in Technology.

Espoo 21.11.2011

Thesis supervisor:

Prof. Antero Arkkio

Aalto University
School of Electrical
Engineering

AALTO UNIVERSITY
SCHOOL OF ELECTRICAL ENGINEERING

ABSTRACT OF THE
MASTER'S THESIS

Author: Deepak Singh

Title: Calorimetric Measurement of the Stator Core Losses Caused by Manufacturing

Date: 21.11.2011 Language: English Number of pages:8+53

Department of Electrical Engineering

Professorship: Electromechanics Code: S-17

Supervisor and instructor: Prof. Antero Arkkio

This thesis is a part of the research on the effect of the manufacturing process on the core losses of the electrical machine. Within this thesis, a special test setup, that has same flux density distribution as the actual machine in no-load, is used to measure only the stator core loss. For this, a slip-ring rotor is designed and constructed. Furthermore, a modified calorimeter is constructed to accurately measure the stator core loss. In order to account only for the stator core loss, the test setup is excited from the stationary rotor which is also thermally isolated from the measurement chamber of the modified calorimeter.

The experimental setup is then operated at various conditions to determine the range of operation having optimal accuracy. After that, the stator core losses at frequencies ranging from 300 Hz to 1 kHz and air-gap flux densities ranging from 0.3 T to 0.4 T, are measured and compared with the results obtained from the FE simulation (FCSMEK). The measured result at almost all the frequencies and the air-gap flux densities is found to be approximately twice of that obtained from the FE simulation. Furthermore, the accuracy of measurement is acceptable for this comparison, but for future study, *i.e.* comparing the difference after the heat treatment, the level of inaccuracy is too high. Thus, few modifications are recommended.

Keywords: Electrical Machine, Core Loss, Manufacturing Effects, Calorimeter

Preface

This research was carried out at School of Electrical Engineering, Aalto University during the period of June 2010 to October 2011. The experimental study was performed utilizing the facilities of the machine hall at Department of Electrical Engineering. I would like to express my sincere gratitude to the *Future Combustion Engine Power Plants* (FCEP) research programme, *CLEEN Oy* for the financial support.

I am extremely grateful to my supervisor Prof. Antero Arkkio for his invaluable assistance, support and guidance. I appreciate the support and encouragement of Prof. Asko Niemenmaa and Adj. Prof. Anouar Belahcen during my research. I would like to acknowledge *Cardo Production Finland Oy* for assisting in the manufacturing of the rotor and *Sundyne Corporation* for providing the stator core. I would also like to thank Mr. Ari Haavisto and Mr. Antti Lehikoinen for their assistance with the work in the lab. My heartfelt gratitude to my work colleagues Paavo, Javier, Bishal and Khang for creating such an amiable working environment.

I am greatly indebted to my mum, dad, sister and brother, for their support, trust and patience. Last but certainly not the least, special thanks to Nepali community at Aalto University; Rajendra, Prajwal, Ujjwal, Ganesh, Manoj, Gautam, Prem, Aditya, Subash, Rupak, Vivek, Aasish and Merina for their continuous support and never ending motivation.

Otaniemi, November 2011

Deepak Singh

Contents

Symbols and Abbreviations

Symbols

A_1, A_2	cross-section area (Appendix B)
B	magnetic flux density
$\hat{B}, B_{\max}$	peak magnetic flux density
$B21, B22, B23$	rotor slot dimensions
C_{d}	coefficient of discharge
c	specific heat capacity
c_p	specific heat capacity at constant pressure
$c_{p,\mathrm{a}}$	c_p of dry air
$c_{p,\mathrm{w}}$	c_p of water vapor
D_1, D_2	inlet pipe diameter and nozzle outlet diameter
d_1, d_2	distance of H-coils from the specimen surface
e_{H}	measured emf (Hall element)
f	frequency
H	magnetic field strength
$H2, H21, H23$	rotor slot dimensions
h_{v}	micro-hardness
i	current
J	current density
K_{Fe}	iron loss correction coefficient
K_{H}	calibration coefficient (H-coil)
K_{tu}	tube leak coefficient
k_{ed}	eddy-current loss coefficient
k_{hy}	hysteresis loss coefficient
l_{ab}	distance between two points a and b
m_{Fe}	iron loss correction coefficient
n	number of turns
P_{Fe}	iron loss
P_{air}	thermal power of air
P_{calib}	power from calibration curve
P_{eddy}	eddy-current power loss
P_{heater}	power of the DC heater
P_{hy}	hysteresis power loss
$P_{\mathrm{stator\ loss}}$	stator power loss
$P_{\mathrm{tube\ leak}}$	power leak from tube
P_{t}	total core loss
$P_{\mathrm{wall\ leak}}$	power leak from wall
p	pressure
p_0	atmospheric pressure
p_1, p_2	upstream and downstream pressure respectively
$p_{\mathrm{a}}, p_{\mathrm{w}}$	partial pressure of dry air and water vapor respectively

p_{ws}	saturation vapor pressure of water
Q_{m}	mass flow rate of air
Q_{v}	volume flow rate of air
R	gas constant
R_{H}	Hall constant
$R_{\mathrm{a}}, R_{\mathrm{w}}$	gas constant of dry air and water vapor respectively
Re	Reynolds number
S	cross-section of coil
T	time period
T_{in}	inlet temperature
T_{rs}	average rotor surface temperature
T_{st}	average stator core temperature
T_{tu}	temperature difference across the tube
t	thickness of Hall element
V	volume
V_1, V_2	upstream and downstream air velocity respectively
V_{H}	voltage induced in H-coil
W_{hy}	hysteresis energy loss
x	specific humidity
Δc_p	error in estimating c_p
ΔK_{tu}	error in estimating K_{tu}
ΔP_{air}	error in estimating P_{air}
$\Delta P_{\mathrm{calib}}$	error in estimating P_{calib}
$\Delta P_{\mathrm{stator\ loss}}$	error in estimating $P_{\mathrm{stator\ loss}}$
$\Delta P_{\mathrm{tube\ leak}}$	error in estimating $P_{\mathrm{tube\ leak}}$
ΔQ_{v}	error in estimating Q_{v}
ΔT_{rs}	error in estimating T_{rs}
ΔT_{st}	error in estimating T_{st}
ΔT_{tu}	error in estimating T_{tu}
$\Delta(\Delta T)$	error in estimating ΔT
ΔT	temperature rise of coolant air
δ	thickness of lamination
ε	expansion factor
ε_p	plastic strain
μ	permeability
ϱ	resistivity
ρ	density
$\rho_{\mathrm{a}}, \rho_{\mathrm{w}}$	density of dry air and water vapor respectively
χ	isentropic coefficient
χ_{rh}	relative humidity

Abbreviations

1-D	One Dimensional
2-D	Two Dimensional
FE	Finite Element
ID	Internal Diameter
NPM	Needle Probe Method
OD	Outer Diameter
PT	Platinum Resistance Thermometer
RC	Rogowski Chattock
RSS	Root Sum Squared
RTD	Resistance Temperature Detector
SRA	Stress Relief Annealing
SST	Single Sheet Tester

1 Introduction

Reduction of the electricity consumption is a major step toward the Global Trend of energy conservation and the environment protection. Ever increasing cost of energy generation and the depleting resources of the conventional fossil fuel drive the innovation towards the efficient energy consumption. As electrical motors are extensively used, from the industrial application to home appliance, reduction of the energy loss in them is of utmost importance. Use of highly efficient non-oriented electrical sheet, have greatly improved the efficiency of modern day electrical machines, still there are rooms for improvement.

Cores of the electrical machines are manufactured from thin laminated electrical steel sheets. The electrical steel sheets are cut to the desired shape (punched or laser cut) and then stacked, pressed and welded to form the final stator and rotor cores. All these manufacturing processes deteriorate the efficiency of the electrical machines by increasing the core losses. Punching and welding of the electrical steel sheets induce shear stress and thermal stress respectively, which in turn impair permeability and hence increase the energy loss. Burrs produced at the cut edges due to punching along with the welding pass, produce interlaminar short-circuit leading to the raised eddy current and thus high losses. Furthermore, pressing and the insertion of core in the casing, exert severe axial and radial stress respectively, which disturb the magnetic flux distribution and hence increase the hysteresis losses. Incorporating these effects due to manufacture processes in Iron Loss Models is very important to accurately predict the core losses of electrical machine. Current industrial practice is to deduce the core losses based on the standard test results, *i.e.* Single Sheet Tester (SST) and Toroidal Tester. However, these standard tests do not include every aspect of the manufacturing effects, thereby underestimate the actual impact.

Studying the manufacturing effects on the core losses of the electrical machines require accurate measurement method. There are a number of proven methods, *i.e.* temperature-time method and calorimetric method, which can accurately measure the losses of the electrical machines, however, segregation of the measured loss to copper and iron loss of both the stator and the rotor is impossible using these methods. Also, there is another method called the field metric method, *i.e.* based on the magnetic measurements, which is good for the core loss prediction but is very much error prone and requires extensive mathematical interpretation. Amongst the measurement methods, the calorimetric method is renowned for its accuracy; still segregation of losses is not possible with the conventional calorimeter. The effects of every step of the manufacturing process, along with different loss measurement and estimation methods are analysed in this thesis. Furthermore, this thesis purposes a method to measure only the stator core loss of the electrical machines and explains in detail a modified calorimetric measurement.

Objectives

The objectives of this thesis are:

i To analyse the effects of the manufacturing process on the core losses of the electrical machine, literature review.

ii To review the different methods of loss measurement of the electrical machine, literature review.

iii To select a suitable measurement method and construct an experimental setup to measure the stator core losses and compare it with the simulated results.

2 Core Losses and Effect of Manufacture Processes

2.1 Core Losses

Machine parts of a rotating electrical machine are subjected to alternating magnetic field. Two distinctive phenomena *i.e.* domain wall motion and swirling eddy current, occur in those machine parts, essentially made of ferromagnetic material, which are also the major sources of core losses and referred as hysteresis losses and eddy current losses respectively.

2.1.1 Hysteresis Loss

In a ferromagnetic material, there are elementary magnets known as Weiss domains. These Weiss domain are separated from each other by Bloch walls, which are transition region at the boundary between magnetic domains [1]. Every Weiss domain consists of a number of atoms perfectly aligned in one direction, so each domain independently is a permanent magnet. The magnetic domains in a ferromagnetic material are placed so that the net magnetic moment of the body is zero. Under the influence of external magnetic field, those magnetic domains already aligned in the direction of external field tend to grow at the expense of non aligned domains, resulting in movement of the domain walls, Figure 1. This continues to a point known as the saturation point on the magnetization curve where all the magnetic domains are aligned and there is minimal increase in the flux for large increase in the field strength.

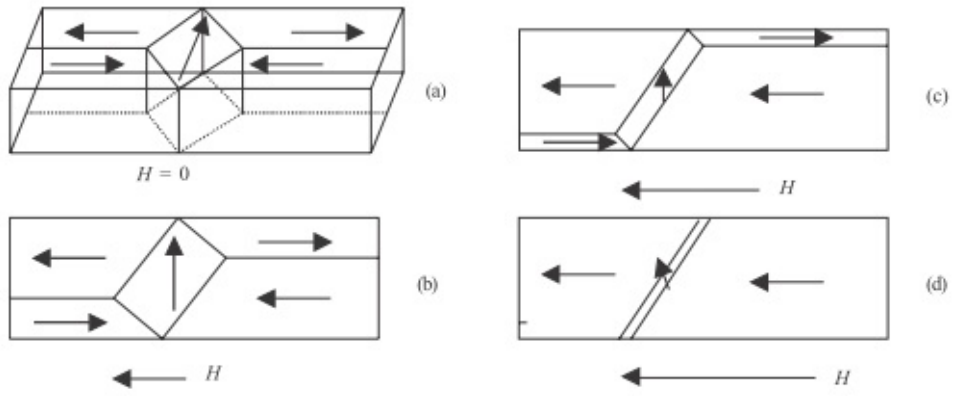

Figure 1: *Domain wall motion. (a) External field strength zero. For (b) and (c) External field strength increases. (d) At saturation*

Once the external magnetic field is removed, not all the magnetic domains return to previous condition, leaving some remanent flux in the body (Figure 2). Energy is consumed by the domain wall movement during magnetization of the body, primarily due to the impurities and heterogeneity present in the body. The amount of energy loss per cycle is given by the area of the hysteresis curve as shown in Figure 3.

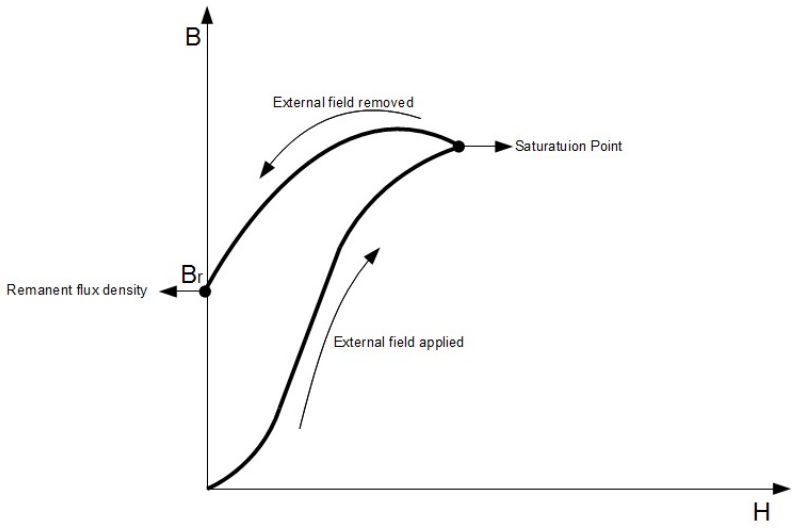

Figure 2: *Saturation point and remanent flux*

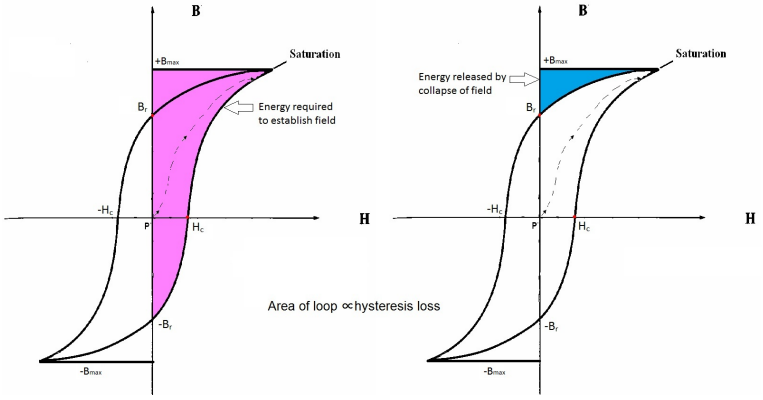

Figure 3: *Hysteresis Loss per cycle*

The integration along the BH-curve, *i.e.* from $-B_{\max}$ to $+B_{\max}$ and back to $-B_{\max}$, gives the total hysteresis energy loss per cycle of the BH-curve, as shown in Equation (1), where V is volume of the body.

$$W_{\text{hy}} = V \int H \, \mathrm{d}B \tag{1}$$

Finally the hysteresis power loss can be calculated by empirical Equation (2), where f is the frequency, n gets a value within the range 1.5-2.5 and k_{hy} is an empirical constant [1].

$$P_{\text{hy}} = k_{\text{hy}} V f B_{\max}^{n} \tag{2}$$

2.1.2 Eddy-Current Loss

Eddy current is produced in a conducting material when placed in time varying magnetic field, as shown in Figure 4 and given by Equations (3) and (4).

$$\nabla \times \vec{E} = -\frac{\partial \vec{B}}{\partial t} \tag{3}$$

$$\vec{J} = \sigma \vec{E} \tag{4}$$

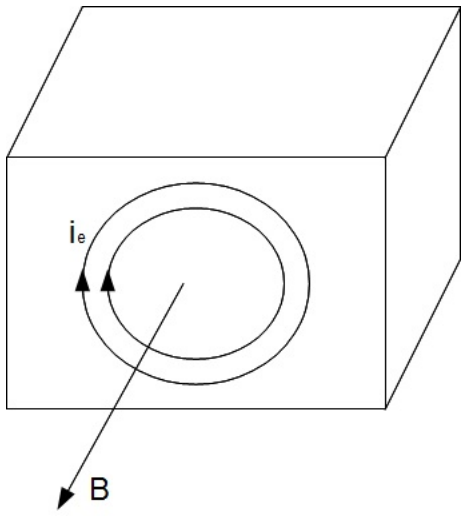

Figure 4: *Eddy current*

Eddy-current loss in the volume of one lamination is given by Equation (5), where V is the volume of the lamination, f is the frequency, $B_{\max}$ is the peak value of the flux density and δ and ϱ are thickness and resistivity of the lamination respectively [1].

$$P_{\text{eddy}} = \frac{V\pi^2 f^2 \delta^2 B_{\max}^2}{6\varrho} \tag{5}$$

Thus we can conclude that eddy current loss is proportional to square of frequency, peak flux density and thickness of the lamination and inversely proportional to resistivity of the material.

$$P_{\text{eddy}} \propto \left(f^2, B_{\max}^2, \frac{\delta^2}{\varrho} \right) \tag{6}$$

2.1.3 Total Core Losses

Manufacturers of electrical steel sheets usually give the losses of material per unit mass at certain peak flux density and frequency. The eddy-current loss and hysteresis loss are not separated. While calculating manually, the magnetic path is divided to n different parts *i.e.* Teeth and Yoke, and the mass of each part is calculated, the total losses are calculated from manufacturer data by Equation (7) [1].

$$P_{\text{Fe}} = \sum_{n} k_{\text{Fe},n} P_x \left(\frac{\hat{B}_n}{x\ T} \right)^2 m_{\text{Fe},n} \tag{7}$$

Where, x and P_x are the induction level and the power losses per unit volume respectively, in manufacturer data. $k_{\text{Fe},n}$ and $m_{\text{Fe},n}$ is the correction coefficient and the mass of n^{th} part respectively. Correction factors for different machines are shown in Table 2.

Table 2: *Correction Coefficient [1]*

Machine type	Teeth	Yoke
Synchronous machine	2.0	1.5 - 1.7
Asynchronous machine	1.8	1.5 - 1.7
DC machine	2.5	1.6 - 2.0

2.2 Effect of Manufacture Processes

Electrical steel sheets undergo different manufacture processes during the making of the cores for electrical machines. Each of these manufacture processes alters physical and magnetic properties of the sheet material. Most common manufacture steps and their effects are discussed below.

2.2.1 Cutting

Electrical steel sheets are cut to a desired shape, which induces strain at the vicinity of cut edge. These induced strains impair permeability and deteriorate the performance of electrical machine by adversely affecting the flux density distribution and increasing losses. There are many methods of cutting; punching and laser cut are common amongst them. The extent of deformation of the crystalline molecular structure depends on many factors of the cutting process and the material properties of the sheet. A worn out cutting tool during punching, slow cutting speed of laser cutting, larger grain size and high silicon content increase the extent of deterioration. Furthermore, the material deformation (burr) right at the cut edge provides an interlaminar short circuit path when stacked together, which increases the eddy-current losses.

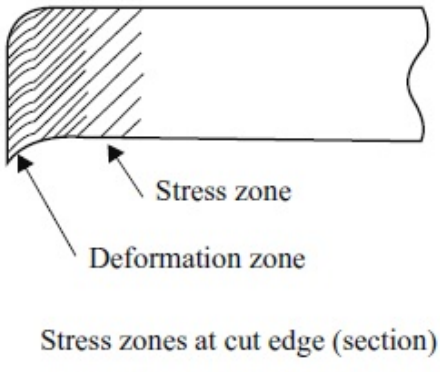

Figure 5: *Burr formation [2]*

There have been many studies regarding the analysis and modeling of induced strain due to cutting. Some of those experimentally analyse the effects of different cutting process. Nakata *et al.* [3] studied the effect of punching and concluded that the degradation of magnetic properties of non-oriented silicon steel sheet due to cutting penetrates up to 10 mm from the cut edge; the deterioration is prominent up to 5 mm from the edge. Similar results were obtained by Moses *et al.* [4], in a different experimental setup. Although both Nakata and Moses used Single Sheet Tester (SST) for their measurement, the type and method of search coil implemented to measure the flux density was different. In both the studies, significant effect due to cutting was observed in the linear region of the BH-curve *i.e.* < 0.5 T. But at the saturation level, *i.e.* at knee of the curve and beyond, the effect due to cutting ceases to exist. Similar was the observation of the study by Arshad *et al.* [5], affirming that the losses do not increase much with the increase in the cut length at higher frequency and induction level. This study also compared losses in samples punched with newly sharpened tool and worn out tool. An increase in losses up to 10% in sample cut by the worn out tool compared to the newly sharpen tool was observed.

Ossart *et al.* [6] attempted to model the induced strain due to cutting by measuring micro-hardness h_{v}. h_{v} is very large at the edge and rapidly decreases with the distance from the edge, as shown in Figure 6. h_{v} is then converted to equivalent plastic strain ε_p by using an established relation between h_{v} and ε_p due to unaxial tensile stress given by Equation (8).

$$h_{\mathrm{v}}(\varepsilon_p) = h_{\mathrm{v},0} + \alpha \varepsilon_p^n \tag{8}$$

where, α and n are the material parameters. Although the model seems to be in good agreement with the experimental result, the authors [6] mentioned that the simplified approach used to convert h_{v} to ε_p is not enough to model the complex phenomena induced by punching.

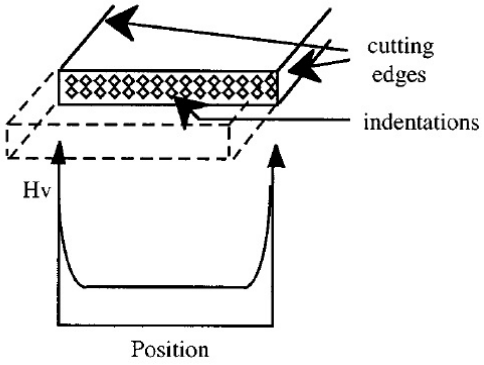

Figure 6: *Principle of micro-hardness measurement and results [6]*

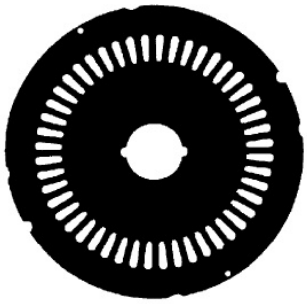

Figure 7: *Sheet geometry (Grid)[7]*

Kedous-Lebouc *et al.* [7] performed a study on a different sheet geometry called the Grid (Figure 7) that best characterized the infuence of punching on the stator teeth magnetic behavior of an electrical machine. The effect of punching on the flux distribution and power loss in the tooth region was studied. Kedous modeled the effect of punching as continuous exponential decrease of the permeability from the center of the tooth to its edges, Equation (9).

$$\mu_{\text{Tooth}} = \mu_{\text{SST}} e^{-\alpha x/d} \quad \text{with } \hat{B} = \mu_{\text{SST}} \hat{H}, \tag{9}$$

Despite high flux density (at which the effect of punching ceases to exist) and relatively small area affected due to punching at the tooth region, an increase in magnetizing current of about 5-10% was observed.
Comparisons between punching and laser cutting have been presented in a study by Kurosaki *et al.* [8]. Contrary to the popular believe, the deterioration of the material is far more significant for laser cut than punching. This can be attributed to the thermal stress induced and the decrease in the resistivity of sheet insulation coating due to the extremely high temperature at the edge during laser cutting. Similarly, Arshad *et al.* [5] concluded that the laser cut losses were higher for low induction level but lower for high induction level compared to the punching and a similar behavior exists for the permeability. However, a study by Baudouin *et al.* [9]

gives an entirely different conclusion based on the X ray characterization of stress (tensor) and the magnetic properties measurement. Baudouin concluded that H, B and μ measurements from the larger specimen prove punching is better than a laser cut, but the measurement of loss (W/kg) was better for laser cut. Also for the small specimens laser cutting was better.

2.2.2 Pressing

Once the sheet is punched to a desired shape, it is stacked and pressed for either welding or inter locking. Pressing the stacked laminations damages the insulation that leads to increased eddy-current loss. Furthermore, pressing might cause material deterioration and increase the hysteresis loss. Arshad *et al.* [5], investigated the effect of pressing and found that the punched core having wide core-back has higher losses than that of narrow core-back. However, no conclusive recommendation was given due to the poor repeatability of the obtained experimental results. The experimental setup is shown in Figure 8.

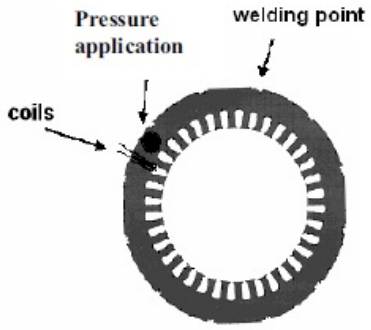

Figure 8: *Stator lamination showing welding and pressing locations [5]*

2.2.3 Clamping

Two most common methods of clamping are welding and interlocking. Interlocking is a process in which a punched depression in one strip is filled by a protuberence from strip above (Figure 10) [2]. These clamping methods (especially welding), along with the burrs produced during cutting form interlaminar short circuit paths for the eddy current and hence raised losses are inevitable.

Study by Schoppa *et al.* [11], found that the increase in losses due to welding is higher for larger grain size of the electrical sheet. Also the short circuit resistance of interlocking is much higher than that of welding, as reported by Kaido *et al.* [12].

Kurosaki *et al.* [8], studied the effect of both the clamping processes on a ring shape specimen that depict the core-back. They deliberately created short circuit paths by welding passes at the inner side of the specimen to simulate the condition of short circuit due to the burrs at cut edge (Figure 11).

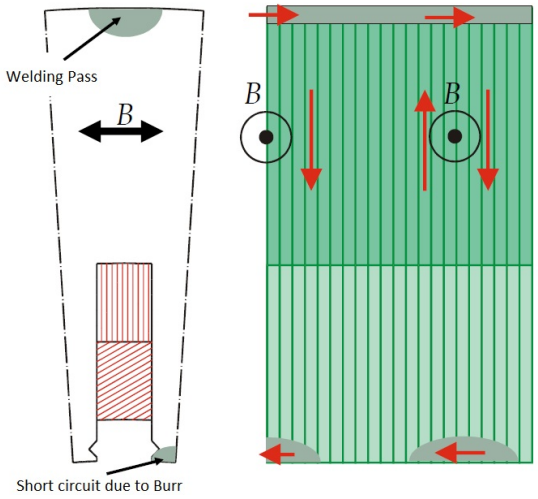

Figure 9: *Interlaminar circulating current [10]*

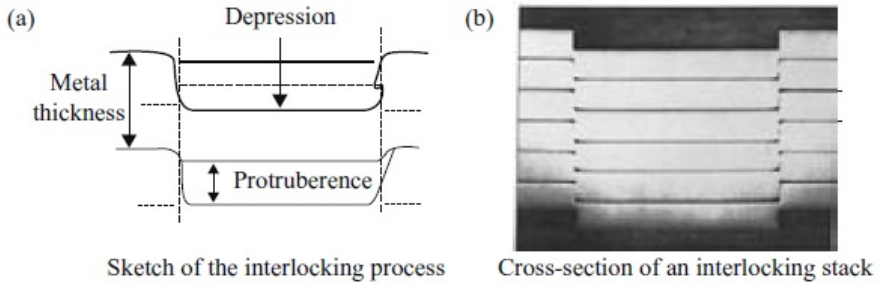

Figure 10: *Details of interlock process [2]*

The interlocked specimens had 3 and 6 interlocking points and the welded specimen had 4 welding passes. The loss in the welded specimen was very high compared to the interlocked specimens and increased extremely with the increasing number of the short circuit welding pass.

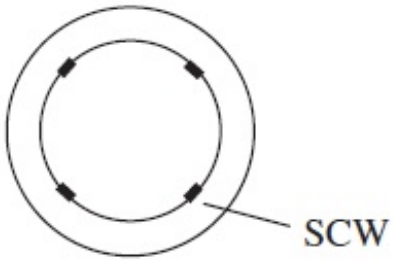

Figure 11: *Schematic view of short circuit welding [8]*

2.2.4 Stress Relief Annealing (SRA)

As the name describes, SRA is done to relieve the residual stress induced during the manufacture processes. Due to the economic constrains, SRA is not a general practice during manufacturing of the cores. SRA involves uniform heating to a pre-determined temperature, holding at this temperature for a period of time followed by uniform cooling. It is very important for the cooling to be uniform otherwise residual stresses equal to or greater than those being relieved may be re-introduced into the material. The pre-determined temperature strictly depends on the type of insulation coat on the lamination, *i.e.* temperature capabilities of inorganic coating is 270 ^{0}C in air and 850 ^{0}C in inert gas but that for organic coating is 180 ^{0}C in air and 500 ^{0}C in inert gas [13]. The additional cost of annealing for improvement of the magnetic properties can only be justified for very narrow laminations [14]. The studies conducted on the effect of cutting [2][3][8][9][15][16], also experimented on SRA samples and found noticeable reduction in the losses compared to non-SRA samples. Figure 12 shows the effect of SRA on the cut edge of grain-oriented 30 mm steel sheet.

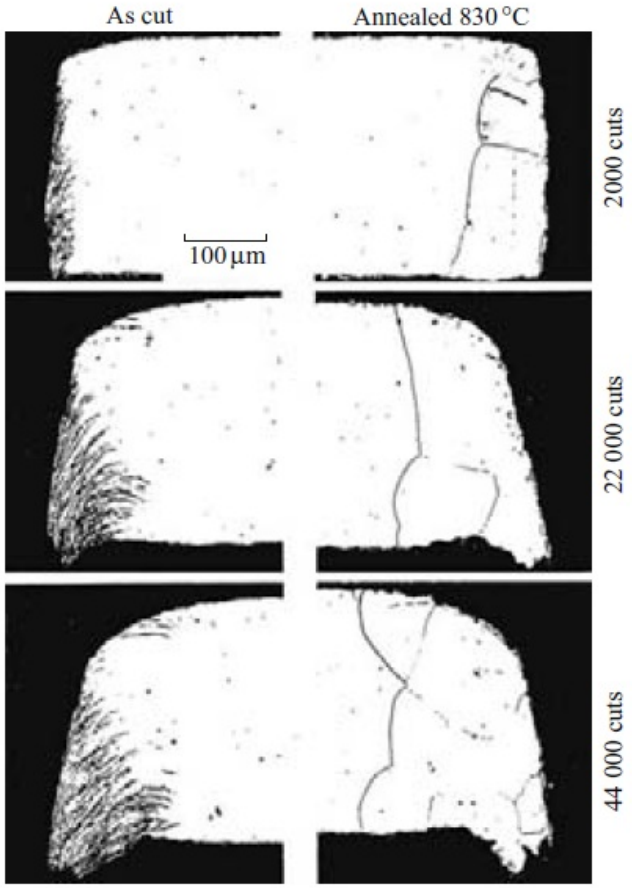

Figure 12: *Effect of worn out tool and SRA [2]*

2.2.5 Casing

The stator cores are hydraulically pressed into cases for the better thermal conductivity between the core and the case. If the cases are heated to facilitate the core insertion and then cooled, this exerts severe radial stress on the stator core. Moses and Rahmatizadeh [17] studied the effect of radial stress on the core of electrical machine. A series of search coils behind the slot and the teeth were used to monitor the effect of radial stress on the flux distribution. Moses and Rahmatizadeh concluded that the radial stress increased the rotational flux behind the teeth and reduced it behind the slot. This disturbance in the flux distribution increased the localized losses behind the teeth. Interestingly, an application of a critical stress of 2 MPa caused increase in loss in all regions of the core.

3 Measurement Methods

In order to study the effect of manufacturing processes, measurement of losses in electrical machine is crucial. Losses in electrical machine can be measured directly as in conventional method of input−output and differential method or by measuring other quantities (like rate of change of temperature and magnetic measurement) and then computing the losses. Selection of a measurement method might depend on following facts:

i Extent of details and type of data required.

ii Accuracy of the measurement method.

iii Practicality of the measurement setup.

Conventional input−output method is inaccurate for the high efficiency electric machine. With the use of non-oriented grade electrical sheets, efficiency of electrical machines has been greatly improved, which means conventional input−output method is highly inaccurate for the loss measurement. Furthermore, both the conventional method and differential method do not provide greater details, *i.e.* do not give the loss distribution across the cross-section of core and segregation of losses (rotor loss, stator loss, friction loss and windage loss), which are required for the study of manufacturing processes effects. Other measurement and computation methods that can be used are presented in Sections 3.1 - 3.3.

3.1 Temperature Time Method

Temperature time method is based on the fact that the loss generated in some part of the machine can be obtained by measuring the energy absorbed or released when the operating conditions are changed. Provided the cooling conditions remain constant for the duration of the test, the initial rate of change of temperature is proportional to the heat input at the measurement point [18].

$$P_{\mathrm{r}} = c\frac{d\theta}{dt} \tag{10}$$

where, P_{r} is the specific core loss in W/kg, c is the specific heat capacity of the material and $d\theta/dt$ is the initial rate of change of temperature obtained from the $Temperature$ v/s $Time$ plot. The major shortcomings of this method are the difficulties of installation and calibration of the thermo sensors and isolation against the surrounding. AJ Gilbert [19] used the temperature time method to obtain the loss distribution across the cross section of a stator core. The thermocouples were soldered to the lamination before the core assembly and the adjacent lamination were slit to bring the leads out (Figure 13). The slitting of the adjacent lamination will gravely affect the local field distribution. With the aim to study the loss distribution at the cut edges, the slitting is unacceptable. Furthermore, the probability of sensor failure is high due to the assembly of core. Also the signals received are noisy and very small in magnitude that requires high quality filters and amplifiers.

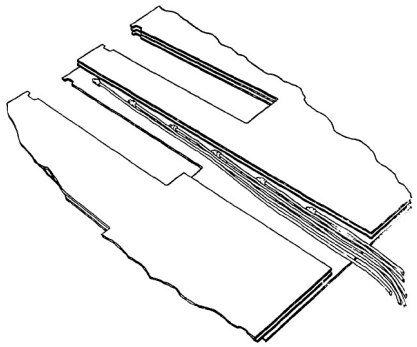

Figure 13: *Arrangement of thermocouples on a stator lamination [19]*

Another possible application of this method to obtain the loss distribution is to implement a Single Sheet Tester (SST) with a specimen and an excitation similar to the actual machine. Once the pattern of loss distribution which also includes the increased loss due to cutting, is obtained, the total core loss can be estimated. Temperature sensors have to be distributed so that the effect of sheet cutting during the manufacture can be studied, *i.e.* very close to cut edges of the tooth and also at the mid of tooth. Thermal imaging can also be used to obtain the temperature distribution, but the resolution of thermal camera must be very high in order to obtain desired accuracy. Moreover the physical surrounding of the specimen does not replicate the actual condition, but still a good estimation of loss distribution can be achieved provided the size of thermal sensor be small enough or the resolution of thermal camera be good enough.

3.2 Field Metric Method

Core loss can also be calculated from the measured magnetic field strength H at the sample surface and the flux density B inside the sample. This method is very accurate and provides greater details of the loss distribution across the cross section of the core. For the evaluation of core loss, Equation (11) is used; where, P_t is the total core loss, T is the time period of magnetization and ρ is the density of the sample.

$$\begin{aligned} P_\mathrm{t} &= \frac{1}{\rho T}\int_0^T \left(\vec{H}.\frac{d\vec{B}}{dt}\right)\,\mathrm{d}t \\ &= \frac{1}{\rho T}\int_0^T \left(H_x\frac{dB_x}{dt} + H_y\frac{dB_y}{dt}\right)\,\mathrm{d}t \end{aligned} \tag{11}$$

Major difficulties with B and H measurement are the manufacture, calibration and installation of the B and H sensors. Some of the widely used methods to measure B and H are presented in Sections 3.2.1 and 3.2.2.

3.2.1 Flux Density (B) Measurement

Search Coil method

The magnetic flux density vector B can be measured in SST using a sensing coil, wound around the whole sample with uniform flux density or threaded through small holes with non-uniform flux density at the position of interest as shown in Figure 14.

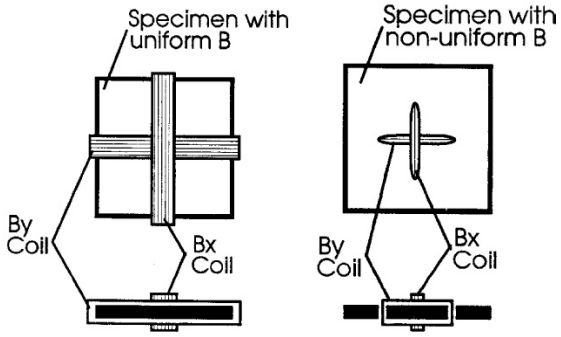

Figure 14: *B coil for specimens with (a) uniform B, and (b) nonuniform B [20]*

The induced voltage over the wound coil is proportional to the magnetic flux density through the coil.

$$B(t) = \left(\frac{1}{nS}\right) \int V \, \mathrm{d}t \tag{12}$$

where, V is the induced voltage, n is the number of turns and S is the cross section of the coil. The lead wires of the search coil are twisted in order to minimize the error due to the stray flux. The search coil method is very effective and accurate in measuring the global magnetic properties, *i.e.* when the distance between the holes is large. But for the local flux density measurement, this destructive method is unreliable because the drilled holes introduce stress which alters the local magnetic properties.

Needle Probe Method (NPM)

The basic principle of NPM is that the eddy current ($\vec{J} = \sigma \vec{E}$) is induced in a steel sheet carrying time varying magnetic flux ϕ, resulting in the potential difference measured by the needle. The contour right below the needle contacts 1234 (Figure 15) encloses the surface area considered by the needles for the flux density measurement *i.e.* $S = \frac{1}{2}td$, where t is the thickness of the sheet and d is the distance between the needles. Maxwell's second equation in the integral form is

$$\oint_C \vec{E}.\vec{dl} = \int_S \vec{B}.\vec{dS} \tag{13}$$

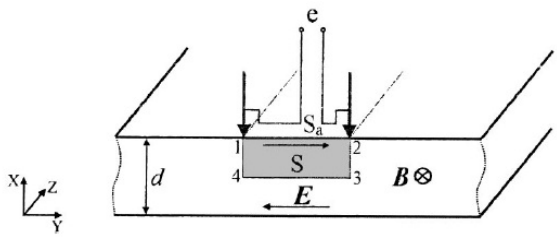

Figure 15: *Principle of NPM [21]*

Evaluating the $\vec{E}.\vec{dl}$ component for 1234, $\vec{E}.\vec{dl}$ is 0 for $1 \rightarrow 4$, $2 \rightarrow 3$ (as E is perpendicular) and $4 \rightarrow 3$ (due to symmetry *i.e.* $\vec{E} = 0$ at the center of lamination). Two conditions have to be fulfilled in order to explain that the needle voltage represents the magnetic flux passing the rectangular area 1234 under the needles. First, flux density B should have only spatial dependency on x and second both the needles are far enough away from the lamination side edge [21]. Both conditions guarantee that the $\vec{E}$ vector is parallel to the surface of the steel sheet. Vertical $\vec{E}$ field component is a major error source, so are the stray air flux coupled with the lead wires and the non-uniform flux distribution due to non-homogeneous material properties. NPM is also prone to the noise interference and requires high quality filters and amplifiers. Accuracy of the NPM is greatly reduced when measuring close to the cut edges, mainly due to the non-homogeneous material at the edges and the vertical $\vec{E}$ field component. This can be explained by drawing a contour that has only the non zero $\vec{E}.\vec{dl}$ component along the surface of the needle contact (Figure 16).

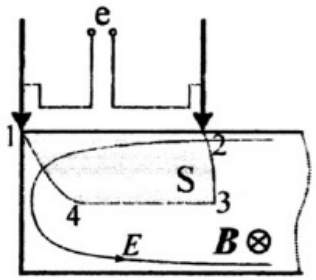

Figure 16: *Influence of the geometrical edge effect [21]*

It is clear from the figure that the area enclosed by the contour is greater than the rectangle below the needle. Thus this method is underestimating the flux through the needles when measuring close to the edge [21]. George Loisos and AJ Moses [22], proposed a modified NPM (Figure 17) and found that error was still very large with the reduced needle separation. Similarly, Abdallh *et al.* [23] proposed another modified NPM to counter the effects of the air flux (Figure 18).

Wulf *et al.* [21], suggested an iterative numerical procedure for the interpretation of the experimental data obtained from the local flux needle probe measurement.

Crevecoeur *et al.* [24], used the space mapping techniques for the reconstruction of the local magnetic properties of the steel sheet by NPM.

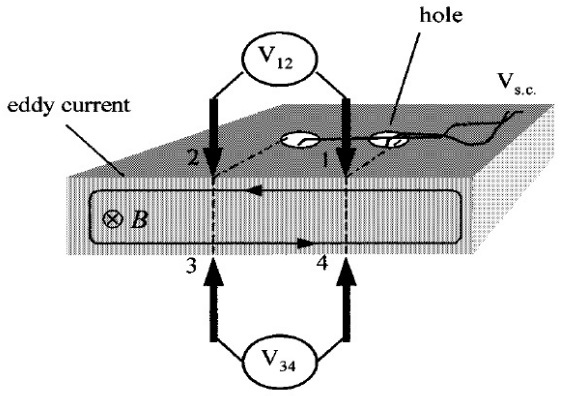

Figure 17: *Search coil and Modified NPM*

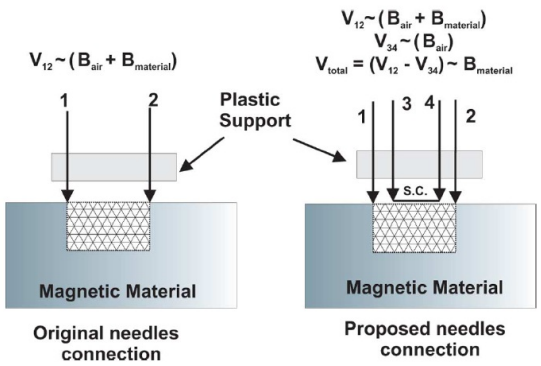

Figure 18: *Modified NPM [23]*

3.2.2 Field Strength (H) Measurement[20][25]

H-Coil

The tangential component of the magnetic field strength at the surface of specimen can be measured by using a search coil placed on the surface (Figure 19).

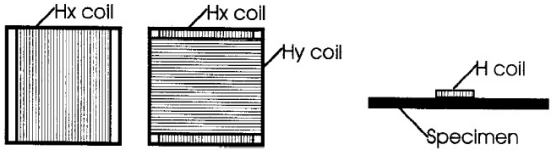

Figure 19: *(a) 1-D H-coil, (b) 2-D H-coil, and (c) position of H coil*

The magnetic field strength can be calculated by following relation:

$$H = \frac{1}{\mu_0 K_{\mathrm{H}}} \int V_{\mathrm{H}} \, \mathrm{d}t \tag{14}$$

where V_{H} is the terminal voltage of the H coil and K_{H} is the calibration coefficient. This method can give accurate measurement of H if the magnetic field is uniform over the specimen surface. In order to reduce the errors, the H-coils must be very thin and placed very close to the surface. This construction and installation requirement for the desired accuracy is often difficult to achieve. So, two H-coils arrangements as shown in Figure 20, can be used to reduced the error due to variation of the magnetic field with the distance above the specimen surface.

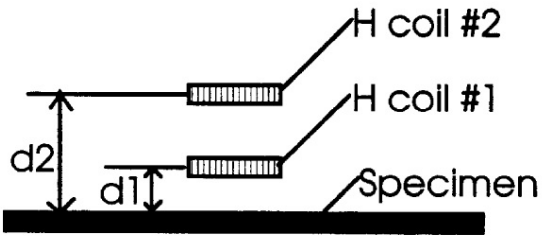

Figure 20: *Two H-coil arrangement*

H can be extrapolated from the obtained data as:

$$H = \frac{d_2 H_{\mathrm{coil}\,1} - d_1 H_{\mathrm{coil}\,2}}{d_2 - d_1} \tag{15}$$

where, $H_{\mathrm{coil}\,1}$ and $H_{\mathrm{coil}\,2}$ are measured field strength of H-coil 1 and H-coil 2, and d_1 and d_2 are the distance of two H-coils from the specimen surface. Linear extrapolation provides fairly accurate result, but the distances d_1 and d_2 should be small.

Rogowski-Chattock Coil (RC coil)

RC coil is also known as the magnetic potentiometer and has higher accuracy than the conventional single H-coil. H can be obtained by time integral of V_{H}, similar to (14). Here, $K_{\mathrm{H}} = A_{\mathrm{H}} l_{ab} n$, A_{H} is the cross section of coil, n is the number of turns per unit length of the coils and l_{ab} is the distance between measuring points A and B (Figure 21).

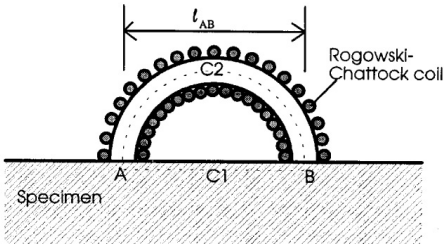

Figure 21: *Rogowski-Chattock coil*

Hall Element

Hall Element works on the principle of the Hall Effect. When a current carrying conductor is placed in a magnetic field perpendicular to the current flow, a voltage called as the Hall Voltage appears transverse to the current, as shown in Figure 22. Hall Effect is prominent in the semiconductors compared to the metals.

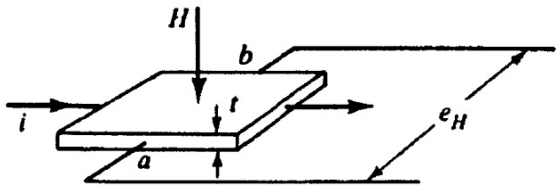

Figure 22: *Relationship between H, current and EMF in the Hall effect*

H can be estimated by (16), where e_{H} is the EMF measured, t is the thickness of the plate, R_{H} is the hall constant which is the property of the material and i is the current through the plate.

$$H = \frac{e_{\mathrm{H}} t}{R_{\mathrm{H}} i} \tag{16}$$

3.2.3 Summary (Field Metric Method)

Being a non destructive process NPM is the only suitable option for the local flux density measurement. However, NPM is error-prone and requires extensive mathematical interpretation in order to derive the magnetic properties from the measured data which is beyond the scope of this thesis. Dimension of all the magnetic field strength sensors (H-coils and sensors) are large, *i.e.* the measured data do not represent the local magnetic measurements. Furthermore, none of the combination of H and B sensors can perform simultaneous measurement at the same point. Enokizono *et al.* [26], used a sensor arrangement combining $2D$ H-coil and NPM, to obtain the simultaneous measurement of H and B at the same place. But still the dimension, that was $15 \times 15\,\mathrm{mm}$, is not suitable to measure the B and H distribution close to the cut edge (tooth region especially).

3.3 Calorimetric Method[27]

Losses in the electrical machines are mostly dissipated as heat, resulting in an increase of the machine temperature above the ambient. Basically, in the calorimetric method a thermally insulated closed chamber is build around the machine and the heat dissipation inside the chamber is measured. The test condition within and immediately adjacent to the test machine should not differ significantly from those of the normal operation, *i.e.* the temperature within the calorimeter chamber should not exceed the specified maximum ambient temperature for the test machine [27]. So, the system requires a method of cooling in order to transport the heat dissipated

by the test machine outside the measuring chamber and hence to maintain a steady ambient test temperature. The power dissipated by the test machine is given by

$$P_{\text{coolant}} = c_p \rho Q_{\text{v}} \Delta T_{\text{coolant}} \tag{17}$$

where, c_p is the specific heat of the coolant, ρ is the density of the coolant. Q_{v} is the flow rate of the coolant and ΔT is the temperature rise of the coolant. By accurately measuring Q_{v} and $\Delta T_{\text{coolant}}$, and assuming other properties of the coolant (c_p and ρ) to be constant over the working temperature range, it is possible to accurately calculate the loss of the test machine using (17).
Based on the method of the heat exchange and the coolant flow, calorimeters are of two types

Open Type

Open type calorimeter draws and exhausts air from the surrounding atmosphere as shown in Figure 23.

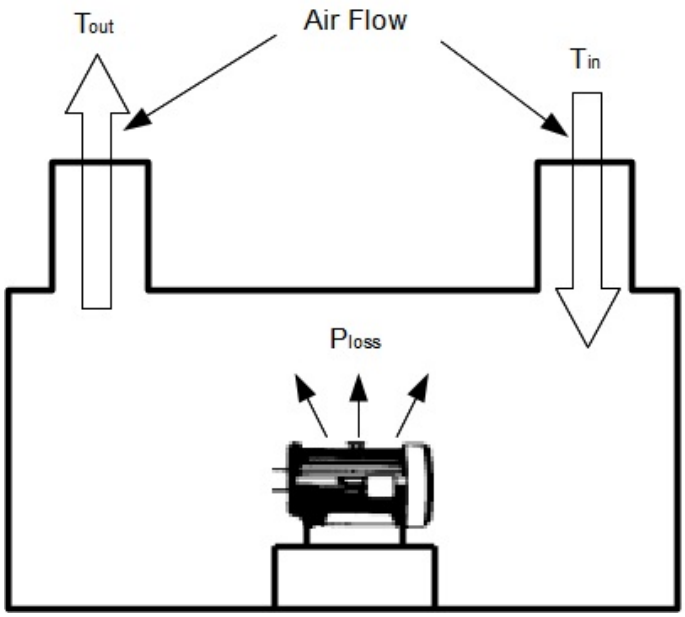

Figure 23: *Open type calorimeter*

The specific heat and the density of atmospheric air depend on the relative humidity and the constituent gasses, and varies with the temperature. Although the specific heat and the density of the coolant air can be assumed constant over the inlet and the outlet, the temperature and the air flow profile varies significantly. In order to determine heat dissipated from the direct measurement, measurement of the relative humidity, the barometric pressure and the atmospheric temperature is required to accurately estimate the density and the specific heat of air. Also, it requires the measurement of flow and temperature profile over the inlet and the outlet, which is very difficult.

Closed Type

There is a secondary coolant (generally water) in the closed type calorimeter and a heat exchanger to dissipate heat from the primary coolant (air) to the secondary coolant. The closed type calorimeter is air tight and the primary coolant circulates either by the natural convection or the internal mounted fan (Figure 24). The heat exchanger and the circulating fan increase the complexity of the measuring chamber.

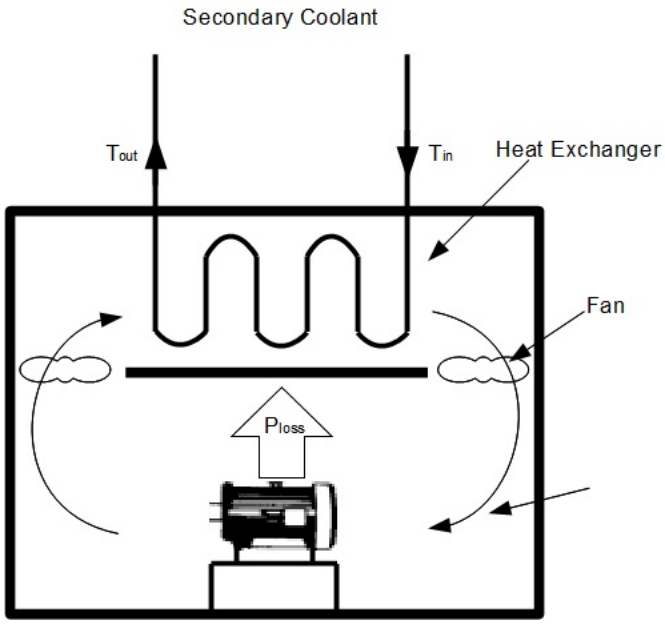

Figure 24: *Close type calorimeter*

Advantage of the close type calorimeter is that unlike the open type, flow and temperature measurement of water is relatively easy, and the variation of the specific heat and the density of water is extremely low over the large working temperature range. However, the time required to reach the steady state for the close type calorimeter is very high compared to the open type calorimeter.

Methods of Operation

A Calorimeter can be operated in three ways, namely direct method, calibration method and balance method. The direct method requires determination of all the possible heat loss from the measuring chamber, *i.e.* heat loss from the wall of the measuring chamber, the metallic base mount of test machine and the shaft of the test machine. The direct method further requires the knowledge of the flow and the temperature profile at the inlet and the outlet, along with the accurate measurement of the relative humidity and atmospheric pressure to determine the exact specific heat capacity of air. While in the calibration method, the measuring chamber is heated up with a known power source and the calibration of the setup is done against temperature rise keeping the flow rate of coolant constant, *i.e.* curve

for heat dissipation is plotted as a function of change in the temperature of coolant at a constant predetermined flow rate of the coolant. After the calibration of the setup, the actual test is conducted at the same flow rate of the coolant and the temperature rise of the coolant is used to determine the losses in the test machine based on the calibration curve. The heat loss from the measuring chamber is assumed to be same for both the calibration test and the actual test. Furthermore, the calibration method also requires the measurement of the relative humidity and the atmospheric pressure that is used along with the calibration curve to determine the heat dissipated.

In the balance method, there are two phases for each measurement. First is the actual test where the motor is operated at the desired load until a steady state is attended, *i.e.* temperature rise of the coolant is constant. Then in the second phase the unexcited motor is rotated by an external DC motor, at the same RPM as during the actual test. This is done to ensure similar flow condition of the coolant in both phases. The chamber is then heated by an alternative heating source and the power dissipated is adjusted to give the temperature rise of coolant similar to the actual test. The accuracy of the balance method is mainly determined by the accuracy of wattmeter connected to the alternative source and the accuracy of temperature measurement system [27]. Humidity and temperature control of the inlet coolant further improves the accuracy of the setup.

4 Experimental Setup

The primary objective of this thesis was to build an experimental setup which could measure the core losses of the stator. Based on the analyses of the loss measurement methods in the previous chapter, the calorimetric measurement method was chosen over the rest. The idea was to produce a rotating magnetic field in the stator core similar to the no-load condition in the actual motor and measure the losses in the stator core. In order to account only for the stator core losses, the system was excited via a thermally insulated rotor, *i.e.* rotor iron and copper loss were isolated from the measuring chamber of the calorimeter. A special rotor and a modified calorimeter were designed and constructed (explained later in this chapter) with the provision to measure many stator cores of similar cross section and at different manufacture stages.

4.1 Rotor Design

In order to create the rotating magnetic field in the stator core, the rotor was designed with proper slots (*i.e.* number and dimension), and appropriate winding configuration, which have been explained in Section 4.1.1. As mentioned earlier, the rotor needs to be thermally insulated, the air gap must accommodate the thermal insulation material. Thus, the rotor was stationary. The thermal insulation of the rotor poise the problem of overheating of the rotor, so a cooling method was designed, as explained in Section 4.1.2.

4.1.1 Electromagnetic Design

The actual machine under consideration was a 1000 Hz, 2-pole, high-speed induction motor. The objective of the rotor design was to produce the same flux density distribution in the stator core as in the no-load operation of the actual machine. However, there were few practical difficulties and the following design considerations were taken into account:

i The air gap (δ) must be large enough to fit the thermal insulation material, in this case it was a 2.5 to 3 mm thick glass fiber tube. However, the magnetizing current required would be very high if the air gap is too large.

ii The effect of circulating current which is detrimental at the higher frequencies, explained later in this section, must be considered. The depth of rotor slot $H2$ and the winding configuration must be appropriately chosen to limit its effect.

iii Input supply required to generate the desired air-gap flux density must comply with the frequency converter output, *i.e.* voltage and frequency must be in the range of frequency-converter output. Thus, the winding configuration must be properly manipulated for this purpose.

Detail dimensions of the designed rotor are shown in Figure 25, Figure 26 and Table 3. The above design was obtained by $FCSMEK$ simulation.

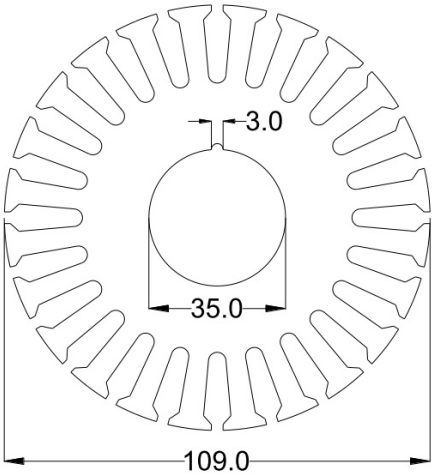

Figure 25: *Rotor cross-section*

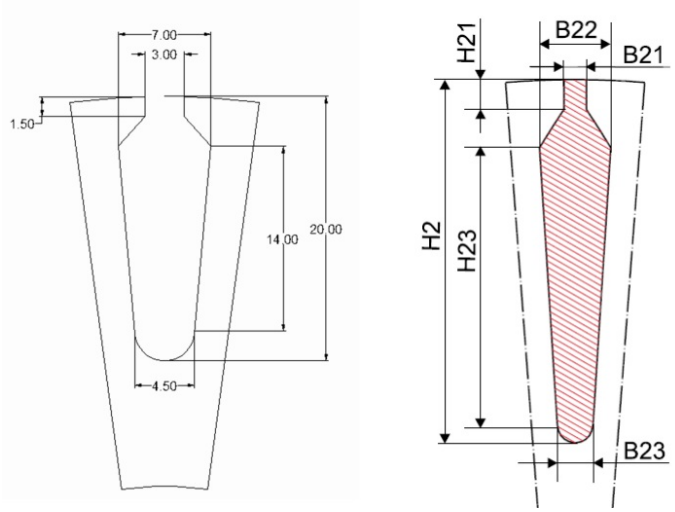

Figure 26: *Rotor slot dimension*

Table 4 shows the stator core losses at 1000 Hz and 0.44 T air-gap flux density *i.e.* the eddy-current loss and the hysteresis loss, of both the actual machine and the test machine. This comparision shows that a rotating magnetic field similar to the actual machine was produced in the test machine. Due to the difference in the rotors of both the machines, *i.e.* the actual machine was a solid rotor type but the test machine was a wound rotor type, higher harmonic components of the eddy-current loss were greater in the test machine. This was caused by the slot harmonics induced because of the slot opening of the wound rotor.

Table 3: *Rotor Design*

Rotor Dimension	
OD of Rotor	109 mm
ID of Rotor	35 mm
Length of Rotor Core	173 mm
Lamination Thickness	0.2 mm
Length of Shaft	1000 mm
Rotor Slot Dimension	
H2	20 mm
H21	1.5 mm
H23	14 mm
B21	3 mm
B22	7 mm
B23	4.5 mm

Table 4: *Stator Core Loss Comparison*

	Actual Machine (Stator Core Losses)		Test Machine (Stator Core Losses)	
Harmonics	Hysteresis (W)	Eddy-current (W)	Hysteresis (W)	Eddy-current (W)
Fundamental	347.945	498.696	349.249	500.565
3	0.005	0.047	0.007	0.062
5	0.702	10.762	1.311	20.098
7	0.255	5.479	0.483	10.362
9	0.001	0.036	0.004	0.099
11	0.066	2.224	0.125	4.213
13	0.04	1.599	0.076	3.046
15	0	0.014	0.001	0.045
17	0.018	0.918	0.034	1.777
19	0.013	0.745	0.025	1.437
21	0	0.009	0	0.025
23	0.007	0.505	0.014	0.979
25	0.006	0.433	0.011	0.837
27	0	0.011	0	0.018
29	0.004	0.32	0.007	0.623
.	.	.	.	.
.	.	.	.	.
.	.	.	.	.
Total	349.08	524.13	351.38	548.72

Circulating Current

The leakage flux passing across the slot and through the conductor inevitably produces eddy-current loss in the conductor. The eddy-current loss, in a round conductor in transversal magnetic field, is proportional to the fourth power of the diameter

of the conductor ($\propto d^4$). In order to reduce the eddy-current loss in the conductor, parallel conductors connected together only at the beginning and at the end of the winding are used [1]. The spatial distribution of the conductor strands forms a closed loop which links with the leakage flux (Figure 27) resulting in the induction of the circulating current. Contribute of the circulating current to the magnetic flux, and thus to the iron losses, is negligible. However, the increase in the resistive loss in the conductors due to the circulating current must be taken into account.

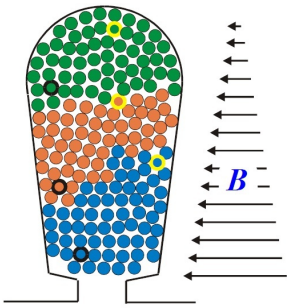

Figure 27: *Circulating current [10]*

Winding Configuration

As mentioned earlier in the design considerations, the winding configuration was done in such a way as to comply with the frequency-converter output. Furthermore, a higher number of turns was preferred in order to limit the effect of circulating current. A higher number of turns implies that the area between the parallel strands (Figure 27) is reduced, consequently reducing the flux linkage and the circulating current. The winding configuration of the designed rotor is shown in Figure 28 and the details have been tabulated (Table 5).

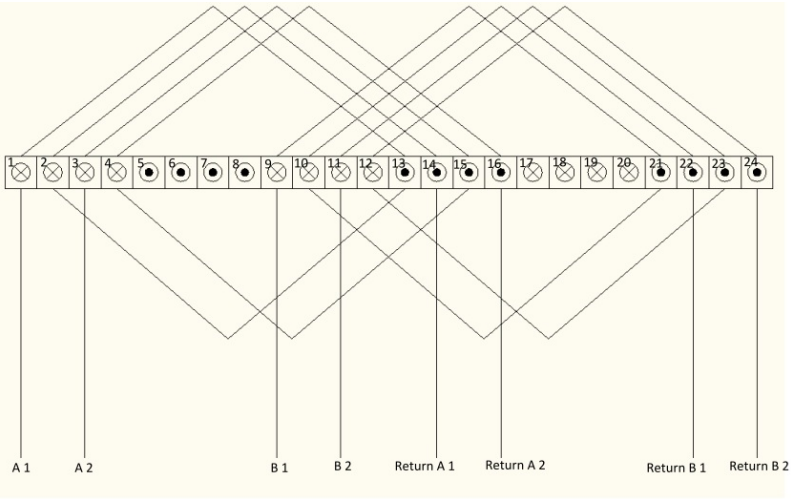

Figure 28: *Winding configuration (Note: similar configuration for the third phase)*

Table 5: *Winding Configuration*

Winding Configuration	
Number of Rotor Slots	24
Number of Phases	3
Number of Parallel Paths	2
Number of Turns in a Slot	6
Number of Layers in Winding	1
Coil Pitch	12
Filling Factor (Area of cooling tube included)	0.3
Filling Factor (Area of cooling tube excluded)	0.541
OD of Cu Wire (single strand)	0.5667 mm
Copper Diameter (single strand)	0.5 mm
Number of Strand per Conductor	27

4.1.2 Cooling Design

The thermal insulation on the rotor causes a problem of overheating of the rotor because of the lack of air flow in the air gap. To maintain the rotor temperature under a safe limit, say 150 ^{0}C, water cooling through the channels in the rotor slots was preferred. Copper tubes (ID 3 mm / OD 4 mm) were used as the water channels in each of the rotor slots (Figure 29) and the flow rate of water in these channels, which was estimated to be 5 ml/sec, was determined by the FE thermal analysis.

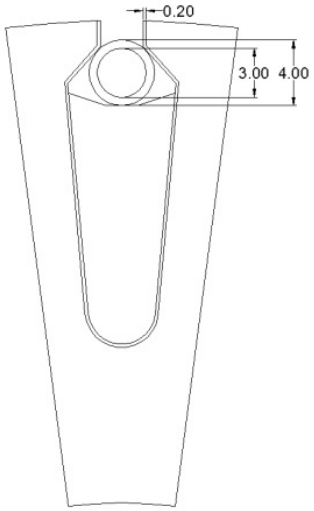

Figure 29: *Rotor slot with cooling channel*

The FE analysis for the cooling of the rotor was done using the General Heat Transfer Module of COMSOL Multiphysics (Figure 30). The heat loss densities for different regions of the rotor, used in the FE thermal analysis, were obtained from the results of FCSMEK simulation, as shown in Table 6 along with the respective thermal conductivities. The results of simulation at 1000 Hz supply were used to determine the

worst case heat loss densities. Moreover, the rotor iron losses were increased 2 times and the rotor copper loss was increased 3 times. This was done to compensate for the increased copper loss due to the circulating current and to ensure proper cooling (and the safety) even at the higher loss densities.

Table 6: *Loss Density and Thermal Conductivity*

	Loss Density (W/m^3)	Thermal Conductivity (W/mK)
Tooth	575285	18
Yoke	708711	18
Winding	1606698	3
FG Tube	0	0.3
Slot Linear	0	0.2
Epoxy Filling	0	0.23
Copper Tube	0	400
Shaft	0	18

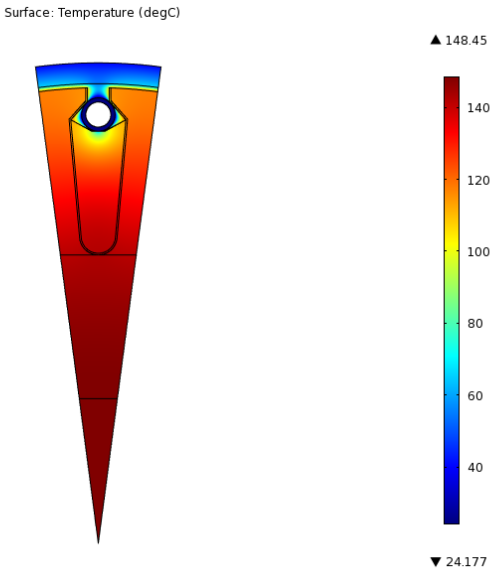

Figure 30: *Thermal analysis of the rotor*

Another area of concern regarding the overheating of the rotor was the end windings. The stationary rotor implies that there was no air flow through the end winding regions, which was further aggravated by the thermally insulating fiber-glass tube. Figure 31 shows a schematic of the end winding cooling. Figure 32 shows the rotor and the final rotor assembly, *i.e.* rotor inside the FG tube.

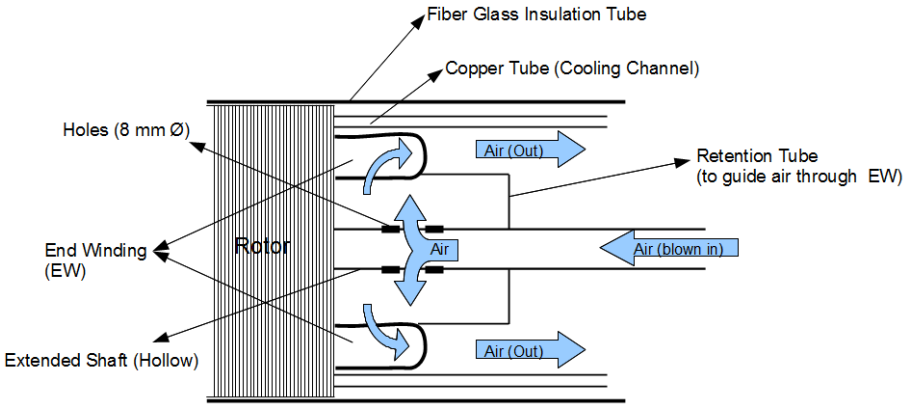

Figure 31: *End winding cooling*

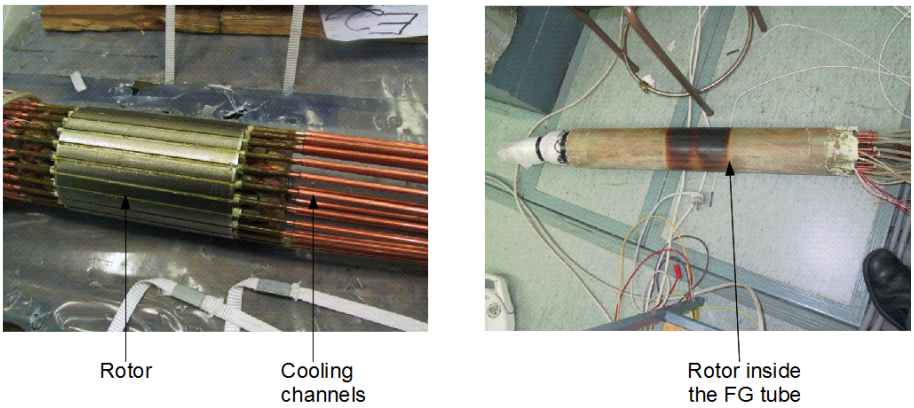

Figure 32: *Rotor assembly*

4.2 Calorimeter Design

A conventional calorimeter for the loss measurement of the electrical machines is not ideal when it comes to segregating the measured loss. A modified calorimeter to measure only the stator core losses has been proposed and constructed. Figure 33 shows the basic plan of the modified calorimeter. Construction, leakage, error analysis and the mode of operation are discussed under this section.

4.2.1 Construction

There are no rigid criteria for the dimensioning of the measurement chamber. The measuring chamber should be big enough to house all the necessary components, but not too large. Large measurement chamber would require longer time to reach the steady state. Also, the chamber should not be too small; the coolant air would not mix properly if the chamber is too small [27]. The measuring chamber constructed had outer surface dimension of $760 \times 650 \times 560\,\text{mm}$ ($L \times B \times H$). The outer insulation wall was made of 50 mm thick polystyrene panels. Furthermore, 1 mm thick aluminum sheet was stuck to inside of the chamber wall in order to have an evenly distributed temperature at the inner surface of the chamber wall.

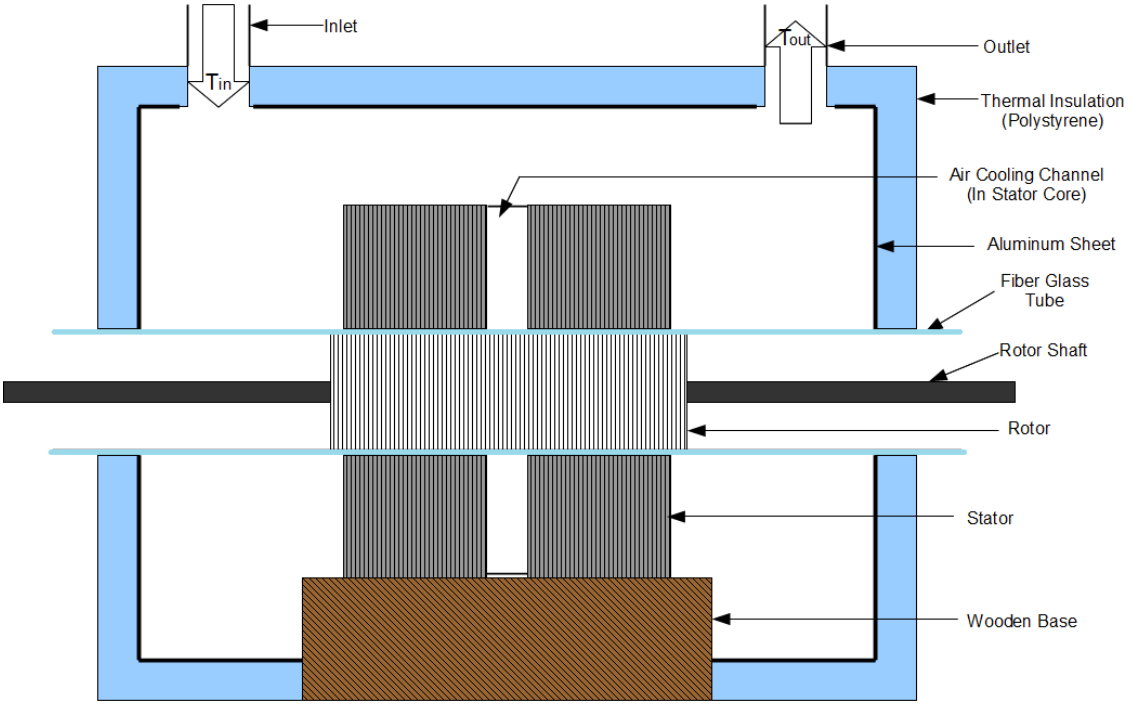

Figure 33: *Modified calorimeter*

A suction pump was used to generate the required rate of the coolant air flow inside the chamber. The heat leakage from the outlet duct, especially before the outlet temperature sensor point, contributes to the measurement error. So, to reduce this measurement error, the outlet duct was also thermally insulated using rock wool. One of the major concerns of a conventional calorimeter is the heat leakage from the chamber via the metallic base mount of the machine. Since the test machine was stationary, *i.e.* vibration and stability was not an issue, the base mount of the test machine was made of wood, thereby reducing the leakage. Figure 34 shows the constructed measurement setup and Figure 35 shows the arrangement inside the measurement chamber. A resign bonded fiber-glass tube of maximum thickness 2.5 mm and internal diameter 109 mm was used to thermally insulate the rotor.

4.2.2 Air Flow and Temperature Rise

The rate of air flow required depends on the maximum ambient temperature around the test machine and the temperature of the machine itself. The temperature within the calorimeter should not exceed a specified maximum ambient temperature of the test machine. Moreover, the stator core temperature must be close to that during the actual operation. The suction pump used to produce the air flow was frequency controlled and had operating range from 0.02 m^3/s to 0.1 m^3/s. A flow nozzle (Appendix B) was used to determine the flow rate of the coolant air.

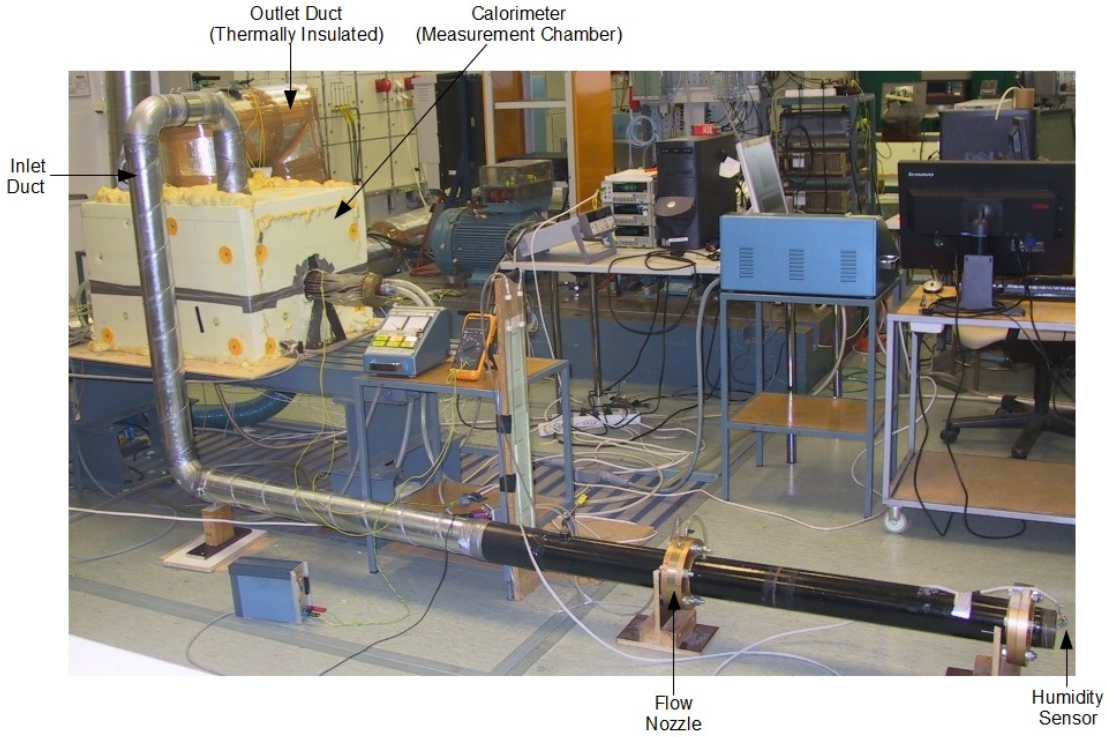

Figure 34: *Experiment setup*

The temperature rise of the coolant air will strictly depend on the temperature within the calorimeter chamber (*i.e.* chamber temperature should not exceed maximum ambient temperature) and the rate of flow of the coolant. However, the type and accuracy of the temperature sensor at the inlet and the outlet will also affect the temperature rise chosen for the coolant air. Resistance Temperature Detectors (RTD) being more accurate than Thermocouple, lower temperature rise of coolant compared to the Thermocouple is possible with the RTD.

4.2.3 Sensors and Instrumentation

Temperature sensors were used for various purposes and at different locations of the measurement setup. Six Platinum resistance thermometers (PT 100) were placed inside the rotor winding (two at both the end windings and two at the vertically opposite slots) to monitor the winding temperature for the safety reasons. In addition, 13 more PT 100 (2 wire connection) were used, out of which 9 were placed at the inner side of the calorimeter chamber in order to monitor the temperature profile inside the chamber and 4 were placed in 10 mm deep holes drilled in the stator core to monitor and obtain the average temperature of the stator core (T_{st}). Similarly, four J-type thermocouples were placed at the rotor surface inside the fiber-glass tube to determine the average temperature at the rotor surface (T_{rs}) which, beside the average stator temperature, is used to determine the temperature difference across the fiber-glass tube (T_{tu}). Furthermore, one PT 100 sensor (4 wire connection) at the inlet and one at the outlet, were used to determine the temperature rise of the

coolant air. The size of PT 100 sensors head ($\approx 20\,\text{mm}$) placed at the center of the inlet and the outlet duct (both $\approx 100\,\text{mm}$ diameter), were large enough for their measurement to be assumed as the avarage temperature over the cross section of the duct.

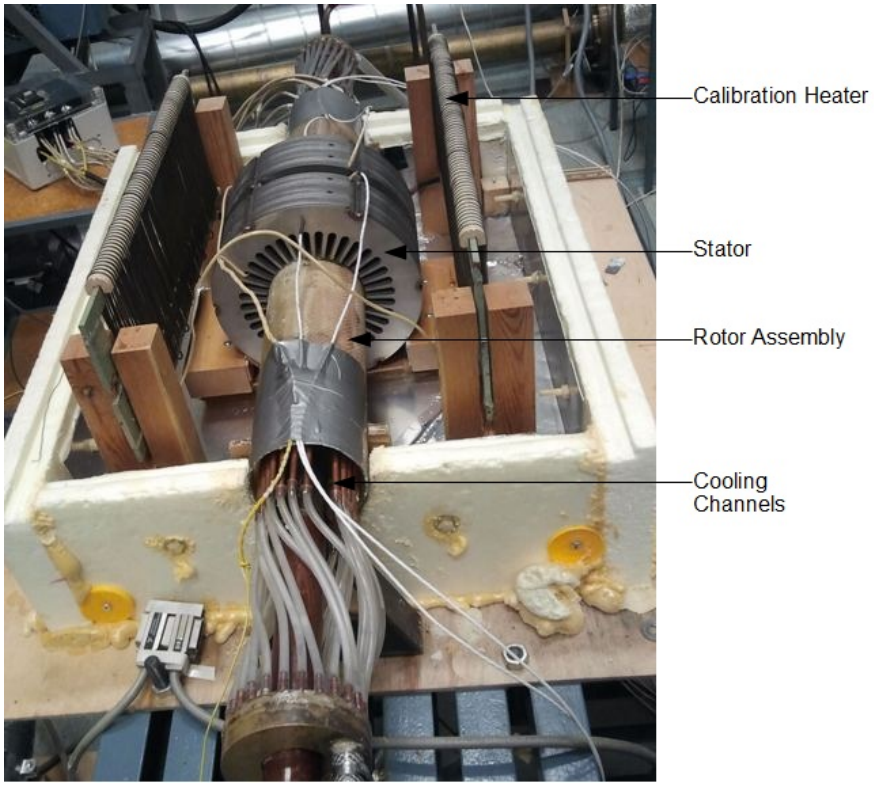

Figure 35: *Measurement chamber*

A temperature compensated capacitive humidity sensor (at the inlet) to measure the relative humidity of the coolant air and an absolute pressure transducers (3.5 bars) to measure the ambient atmospheric pressure were used. The relative humidity, atmospheric pressure along with the ambient air temperature were used to determine the specific heat and the density of the air (Appendix A). A differential pressure sensor was used to measure the pressure drop over the flow nozzle, which is required to determine the flow rate of the coolant air (Appendix B). Also, a single turn search coil was placed at the stator yoke (stator core back) to monitor the induction level based on the voltage induced in the coil. Furthermore, one Agilent 34970A data logger was used for data acquisition of all the thermo sensors, 3 Fluke 8842A multimeters were used to measure the output voltage (DC) of the relative humidity sensor, the absolute pressure sensor and the differential pressure sensor. A Norma D 6100 power analyser was used to measure the heater power during the calibration and also to measure the supply voltage and frequency of the test machine during the actual measurement.

4.2.4 Mode of Operation

Once the assembly of the setup was completed, the test machine was excited at different frequencies and desired air-gap flux densities. The rotor surface temperature was found to be lower than the stator core temperature (at all frequencies and air flow rate) by considerable margin. Furthermore, it was impossible to replicate the exact temperature difference across the fiber-glass tube during the calibration and the balance test. This observation led to the rejection of the balance method of operation. Finally, combination of the calibration method along with accurate estimation of the fiber-glass tube leakage was selected as the mode of operation.

First of all, calibration of the set up was done at different flow rates. During the calibration, two heating elements connected in series and supplied by a constant DC voltage source, were used as the alternate heat source. Also, the flow rate of the coolant air was more or less maintained constant by the frequency converter controlled suction pump. The accuracy of calibration depends on the accuracy of the power meter connected to the alternate heat source, which was about $\pm 1\,\mathrm{W}$. The calibration curve of the setup at different flow rates (used during the actual measurement) is presented in Figure 36.

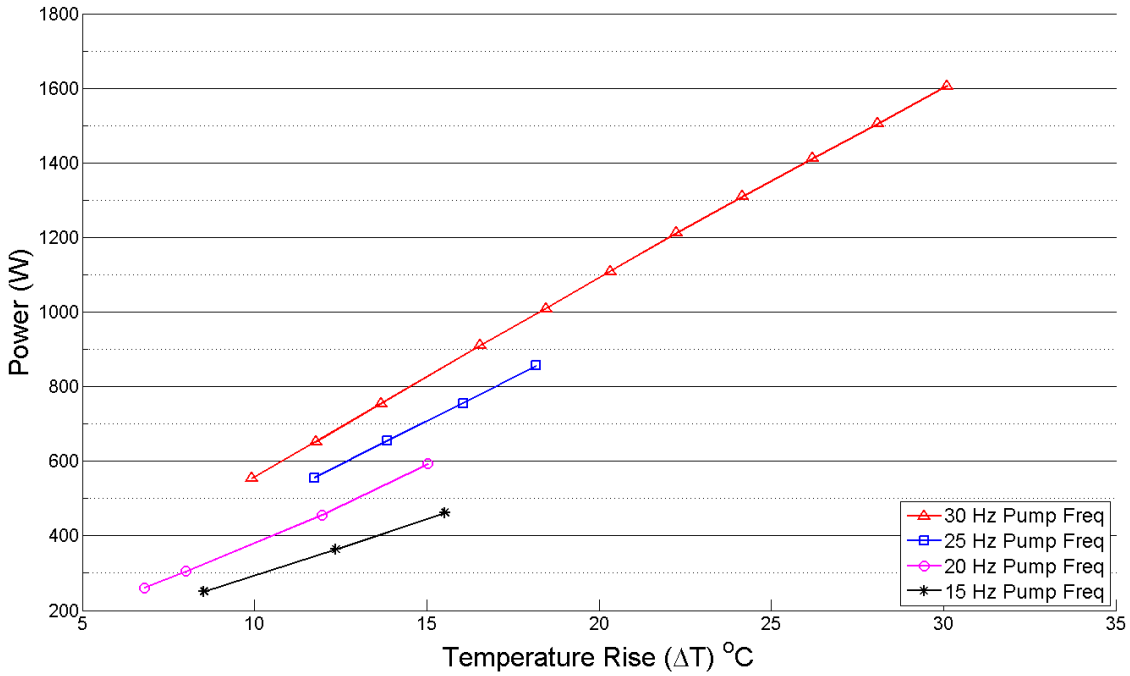

Figure 36: *Calibration Curve*

After the calibration, the actual measurement was done at the calibrated flow rates of the coolant air. Depending on the temperature rise of the coolant air, the stator core losses at various operation points were determined from the calibration curve.

$$\begin{aligned} P_{\text{heater}} &= P_{\text{air}} + P_{\text{wall leak}} + P_{\text{tube leak}} \\ P_{\text{calib}} = P_{\text{heater}} &\approx P_{\text{air}} + P_{\text{wall leak}} \end{aligned} \tag{18}$$

For the calibration, the heat leak through the fiber-glass tube was negligible as the maximum temperature difference across the fiber-glass tube during the calibration ($T_{\text{tu}} = T_{\text{st}} - T_{\text{rs}}$) was less than 4°C. Assuming the temperature profile of the inside wall of the measurement chamber to be similar during both calibration and actual measurement, for the actual measurement,

$$P_{\text{stator loss}} = P_{\text{air}} + P_{\text{wall leak}} + P_{\text{tube leak}}$$

From the calibration curve,

$$P_{\text{stator loss}} \approx P_{\text{calib}} + P_{\text{tube leak}} \tag{19}$$

However, the temperature difference across the fiber-glass tube is significantly high. Thus, the tube leak for the actual measurement was estimated (Section 4.2.5).

4.2.5 Heat Leakage

Leakage through the fiber-glass tube is a major source of leakage during the actual measurement, which requires accurate estimation. Estimation based on the thermal conductivity of the resign-bounded fiber-glass material was inconclusive and experimentally unverified. A number of measurements at different conditions were conducted, which were used along with the measured temperature difference across the fiber-glass tube and the calibration curve, to account for the tube leak.

Based on the observed temperature difference across the fiber-glass tube, the tube leak can be expressed as

$$\begin{aligned} P_{\text{tube leak}} &= K_{\text{tu}} T_{\text{tu}} \\ T_{\text{tu}} &= T_{\text{st}} - T_{\text{rs}} \end{aligned} \tag{20}$$

where, K_{tu} is the leak coefficient of the fiber-glass tube expressed in watt per degree celcius of the temperature difference across the fiber-glass tube, T_{tu} is the temperature difference across the fiber-glass tube and T_{st} and T_{rs} are the stator temperature and the rotor surface temperature respectively.

Two consecutive measurements were done with the same supply frequency and current (*i.e.* stator loss almost equal) but different rotor temperature. The rotor surface temperature was controlled by feeding the cooling channels with cold water and then with hot water (however, this control was very limited). K_{tu} can be estimated as

$$\begin{aligned}
{}^1P_{\text{stator loss}} &= {}^1P_{\text{calib}} + {}^1P_{\text{tube leak}} \\
{}^2P_{\text{stator loss}} &= {}^2P_{\text{calib}} + {}^2P_{\text{tube leak}} \\
{}^1P_{\text{stator loss}} &= {}^2P_{\text{stator loss}} \\
{}^1P_{\text{calib}} + {}^1P_{\text{tube leak}} &= {}^2P_{\text{calib}} + {}^2P_{\text{tube leak}} \\
{}^2P_{\text{calib}} - {}^1P_{\text{calib}} &= {}^1P_{\text{tube leak}} - {}^2P_{\text{tube leak}} \\
{}^1P_{\text{tube leak}} - {}^2P_{\text{tube leak}} &= K_{\text{tu}}\,{}^1T_{\text{tu}} - K_{\text{tu}}\,{}^2T_{\text{tu}}
\end{aligned}$$

$$K_{\text{tu}} = \frac{{}^2P_{\text{calib}} - {}^1P_{\text{calib}}}{{}^1T_{\text{tu}} - {}^2T_{\text{tu}}} \tag{21}$$

where superscripts 1 and 2 represent measurements with cold water and hot water through the cooling channel respectively. The procedure explained above was used to determine the leak coefficient of the fiber-glass tube (K_{tu}) at different stator core temperatures ($T_{\text{st}} \in [80,\ 200]\,^0$C). Also, the measurements were done twice to ensure repeatability and validate the obtained result. K_{tu} obtained was then used to determine the tube leak during the actual measurement. The values of the fiber-glass tube leak coefficient (K_{tu}) obtained experimentally at different stator temperatures, are shown in Table 7.

Table 7: *Tube Leak Coefficient*

Stator Temperature (^{0}C)	K_{tu} (W/^{0}C)
163	4.87
145	4.48
134	4.48
124	4.58
105	4.48
84	3.71

4.3 Error Evaluation

The root sum squared (RSS) method was used for the overall error calculation as explained in Appendix C. The combined uncertainty of sensors was calculated and summarized in Table 8.

Table 8: *Combined Uncertainty*

Sensor	Random Error	Instrument Error	Calibration Error	Combined Uncertainty	Unit
PT100 4-Wire	0.01	0.06	0.15+0.002$\mid T \mid$	-	^{0}C
PT100 2-Wire	0.015	0.06	0.15+0.002$\mid T \mid$	-	^{0}C
Thermocouple J-Type	0.03	1.2	2.20	2.51	^{0}C
Differential Pressure Sensor	2.51	0.63	12.83	13.09	Pa
Absolute Pressure Sensor	2.3	10.00	844.60	844.66	Pa
Relative Humidity Sensor	0.1	0.02	3.50	3.50	$\%\chi_{\mathrm{rh}}$

Note: The instrument error of Fluke Meter was determine by taking the resolution 0.001 V and that of Agilent (used for the temperature sensors) was taken from the specifications of the instrument.

From relation 18 and 19 and assuming the wall loss to be equal, uncertainty in the stator loss estimation is

$$\Delta P_{\mathrm{calib}} \approx \Delta P_{\mathrm{air}} \tag{22}$$

$$\Delta P_{\mathrm{stator\ loss}} = \Delta P_{\mathrm{calib}} + \Delta P_{\mathrm{tube\ leak}} \tag{23}$$

where, $\Delta P_{\mathrm{calib}}$, ΔP_{air}, $\Delta P_{\mathrm{tube\ leak}}$ and $\Delta P_{\mathrm{stator\ loss}}$ are the errors in estimating power from the calibration, the thermal power of air, the fiber-glass tube leak and the stator loss respectively. The propagation of the measurement errors of p_0, χ_{rh} and T_{in} to ΔP_{air} or to $\Delta P_{\mathrm{calib}}$ is negligible compared to the error associated with the difference in the atmospheric condition during the calibration and the actual test. The measured parameters that represent the difference in the atmospheric condition are

$$T_{\mathrm{in,diff}} = T_{\mathrm{in,act}} - T_{\mathrm{in,calib}}$$
$$P_{0,\mathrm{diff}} = P_{0,\mathrm{act}} - P_{0,\mathrm{calib}}$$
$$\chi_{\mathrm{rh,diff}} = \chi_{\mathrm{rh,act}} - \chi_{\mathrm{rh,calib}}$$

where, the subscript *act*, *calib* and $diff$ denote the measured values during actual test, calibration and the difference respectively. The error in c_p, ρ and Q_{v} due to difference in the atmospheric condition during the calibration and the actual test can again be estimated using Sequential Perturbation Method (Appendix C).

Consequently, the ΔP_{calib} can be estimated using the RSS method

$$
\begin{aligned}
c_p &= f\left(T_{\text{in}}, p_0, \chi_{\text{rh}}\right) \\
\Delta c_p &= \sqrt{\left(\Delta c_{p,\ T_{\text{in,diff}}}\right)^2 + \left(\Delta c_{p,\ p_{0,\text{diff}}}\right)^2 + \left(\Delta c_{p,\,\chi_{\text{rh,diff}}}\right)^2}
\end{aligned}
$$

$$
\begin{aligned}
\rho &= f\left(T_{\text{in}}, p_0, \chi_{\text{rh}}\right) \\
\Delta \rho &= \sqrt{\left(\Delta \rho_{\,T_{\text{in,diff}}}\right)^2 + \left(\Delta \rho_{\,p_{0,\text{diff}}}\right)^2 + \left(\Delta \rho_{\,\chi_{\text{rh,diff}}}\right)^2}
\end{aligned}
$$

$$
\begin{aligned}
Q_{\text{v}} &= f\left(dp, p_0, T_{\text{in}}, \chi_{\text{rh}}\right) \\
\Delta Q_{\text{v}} &= \sqrt{\left(\Delta Q_{\text{v},\,\Delta dp}\right)^2 + \left(\Delta Q_{\text{v},\,T_{\text{in,diff}}}\right)^2 + \left(\Delta Q_{\text{v},\,p_{0,\text{diff}}}\right)^2 + \left(\Delta Q_{\text{v},\,\chi_{\text{rh,diff}}}\right)^2}
\end{aligned}
$$

$$
\begin{aligned}
P_{\text{calib}} &= f(c_p, \rho, Q_{\text{v}}, \Delta T) \\
\frac{\Delta P_{\text{calib}}}{P_{\text{calib}}} &= \sqrt{\left(\frac{\Delta c_p}{c_p}\right)^2 + \left(\frac{\Delta \rho}{\rho}\right)^2 + \left(\frac{\Delta Q_{\text{v}}}{Q_{\text{v}}}\right)^2 + \left(\frac{\Delta\left(\Delta T\right)}{\Delta T}\right)^2}
\end{aligned} \tag{24}
$$

Similarly, from equation 21, using 24 and the propagated error (Appendix C), ΔK_{tu} and $\Delta P_{\text{tube leak}}$ can be calculated as

$$
\frac{\Delta K_{\text{tu}}}{K_{\text{tu}}} = \sqrt{\left(\frac{\Delta^1 P_{\text{calib}}}{{}^1P_{\text{calib}}}\right)^2 + \left(\frac{\Delta^2 P_{\text{calib}}}{{}^2P_{\text{calib}}}\right)^2 + \left(\frac{\Delta^1 T_{\text{tu}}}{{}^1T_{\text{tu}}}\right)^2 + \left(\frac{\Delta^2 T_{\text{tu}}}{{}^2T_{\text{tu}}}\right)^2}
$$

$$
\frac{\Delta P_{\text{tube leak}}}{P_{\text{tube leak}}} = \frac{\Delta K_{\text{tu}}}{K_{\text{tu}}} + \frac{\Delta T_{\text{tu}}}{T_{\text{tu}}} \tag{25}
$$

where,

$$
\Delta T_{\text{tu}} = \sqrt{\left(\Delta T_{\text{st}}\right)^2 + \left(\Delta T_{\text{rs}}\right)^2}
$$

Finally, using equations 24 and 25 the overall error in estimating the stator loss ($\Delta P_{\text{stator loss}}$) is given by

$$
\Delta P_{\text{stator loss}} = \Delta P_{\text{calib}} + \Delta P_{\text{tube leak}} \tag{26}
$$

5 Results

The operation points of the test machine, *i.e.* supply voltage and frequency, were determined from the FCSMEK simulation. 0.4 T, 0.35 T and 0.3 T of the air-gap flux densities were chosen for the study. Beyond this limit, either the frequency-converter output did not comply with the test machine's input requirement, or the DC-link voltage of the frequency-converter was exceeding the safety limit. The details of measurements, estimations and errors, are tabulated in Appendix D. The results obtained from the measurement are shown in Figures 37, 38 and 39 and tabulated in Table 9, 10 and 11.

Table 9: *Stator Core-Losses at* $\hat{B}_{\text{air-gap}} = 0.4\,\text{T}$

Frequency (Hz)	Core 1 (W)	Core 2 (W)	Core 3 (W)	Simulated (W)
1000	1739	1721	1773	908
900	1482	1473	1513	772
800	1272	1203	1290	638.5
700	1073	1000	1068	520
600	908	845	851	416
500	669	677	680	314
400	554	468	526	231
300	356	278	362	156

Table 10: *Stator Core-Losses at* $\hat{B}_{\text{air-gap}} = 0.35\,\text{T}$

Frequency (Hz)	Core 1 (W)	Core 2 (W)	Core 3 (W)	Simulated (W)
1000	1444	1407	1437	712.5
900	1243	1175	1237	600
800	1051	983	1052	505
700	875	821	870	414
600		684		325.5

Table 11: *Stator Core-Losses at* $\hat{B}_{\text{air-gap}} = 0.3\,\text{T}$

Frequency (Hz)	Core 1 (W)	Core 2 (W)	Core 3 (W)	Simulated (W)
1000	1106	1086	1095	534
900	950	926	947	452
800	792	763	781	380
700	649	625	661	307
600		518		245

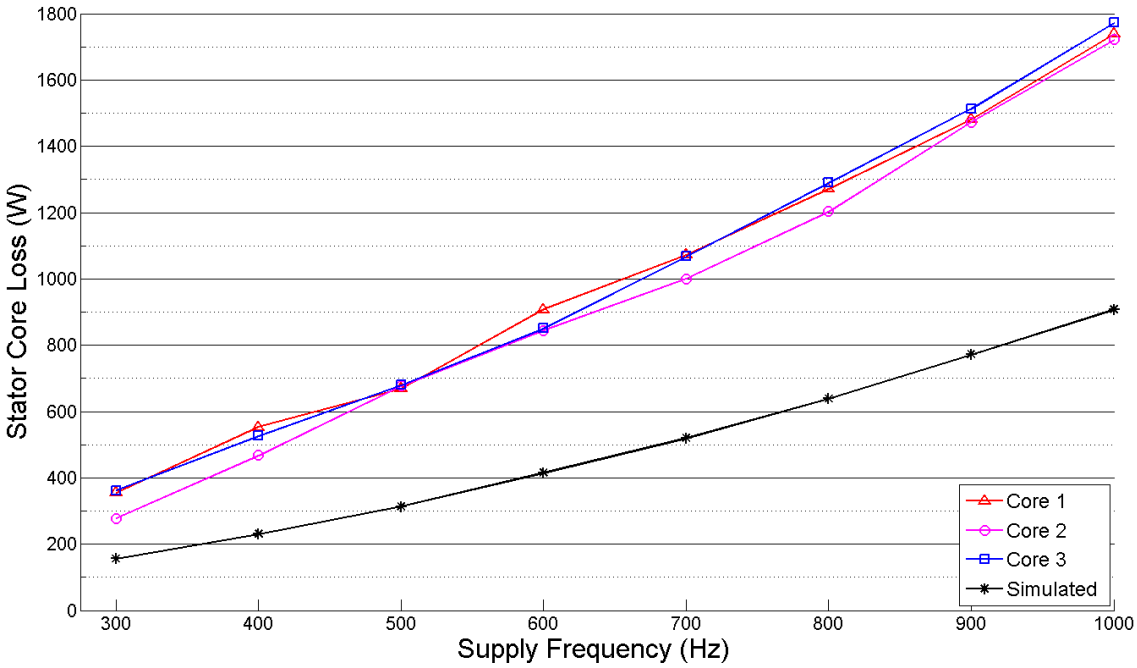

Figure 37: *Stator core loss at* 0.4 T

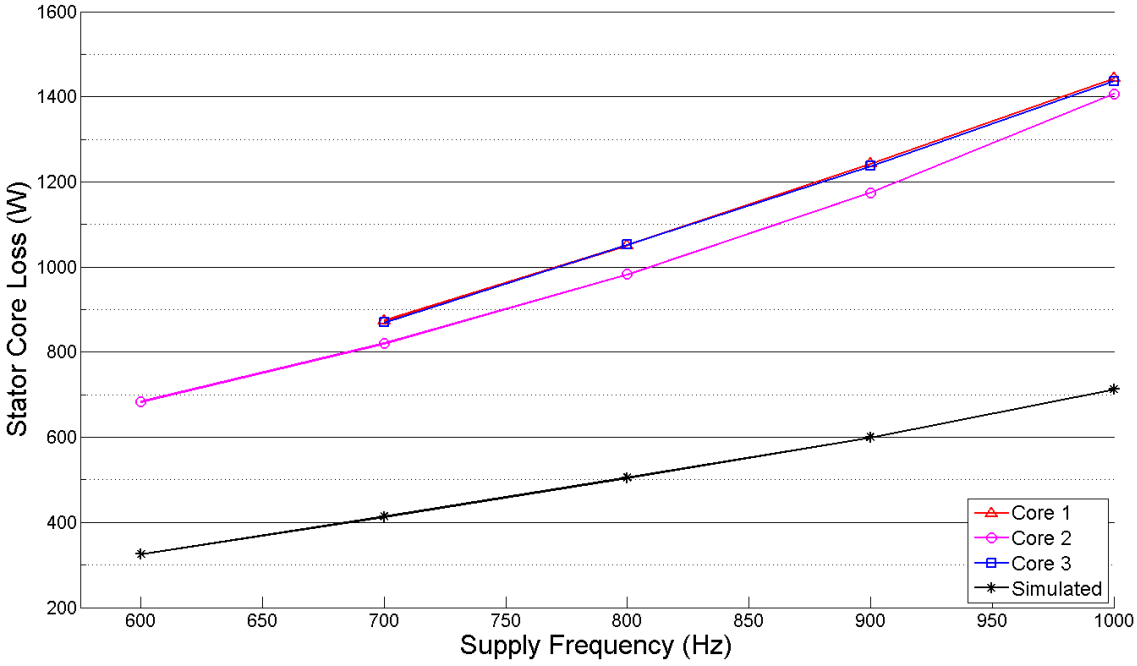

Figure 38: *Stator core loss at* 0.35 T

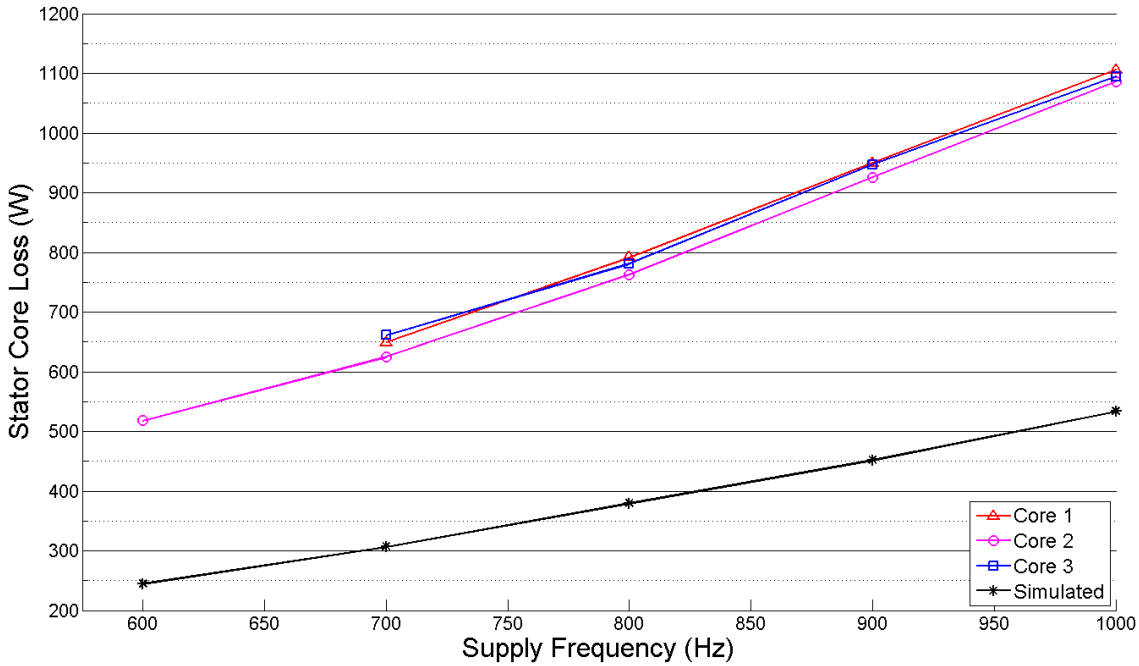

Figure 39: *Stator core loss at* 0.3 T

The measured stator core losses are found to be approximately twice the simulated results at all operational points. With this setup and measurement method, it is not possible to separate the hysteresis loss and the eddy-current loss from the measured losses (Section 6) and to distinguish the major contributor to the increased losses. However based on the measured losses, it is possible to optimized the loss coefficients, *i.e.* hysteresis loss coefficient k_{hy} and eddy-current loss coefficient k_{ed}, which is the future task of this project. Anyway, a generalized conclusion cannot be drawn on the increased core losses dependency on the supply frequency and the flux density, due to the sparse data and narrow range of the air-gap flux densities.

6 Discussion and Conclusion

From the measurement (Appendix D), it is clear that there are some issues concerning the accuracy of the results. Analysing the individual error contribution, it can be argued that the humidity (χ_{rh}) and the temperature (T_{in}) control of the inlet air can reduce the error in thermal power of air obtained from the calibration ($\Delta P_{\mathrm{calib}}$). However, this improvement is insignificant compared to the error due to the power leak through the fiber-glass tube. Although, the experimental estimation of the heat leakage through the tube has been done, it is not worth discussing the methods of reducing the errors associated with this estimation. Instead, some modification in the setup will altogether eliminate the need to estimate the heat leakage through the tube. If during the calibration, the temperature gradient across the fiber-glass tube (T_{tu}) can be maintained similar to the actual measurement, it will effectively be the balanced method of calorimetric measurement (Section 3.3). Thus, the error due to the tube leak will be eliminated. This can be achieved by placing the alternating heat source (DC heater) either inside the stator slots or in good thermal contact with the stator core-back. Such an arrangement will also eliminate the error in assuming equal chamber wall leak during the calibration and the actual measurement. The variation in the wall leak, although trivial, is due to difference in position and temperature of the heat source during the calibration and the actual measurement. Another possible way is to change the entire heat transfer mechanism to water cooling of the stator core. Unlike the closed type calorimeter, the heat exchanger is in contact with the stator core, thus time required to attend a steady state will reduce considerably. Moreover, the cooling must be very effective, with the possibility of better flow control and thus good control of the stator core temperature. Control of the stator temperature will allow the net temperature gradient across the fiber-glass tube to be adjusted to zero, which implies negligible heat leak through the tube. Furthermore, the specific heat capacity and density of water is almost constant over a wide range of temperature and the water flow rate measurement is easy and accurate. Thus, the error regarding the flow rate measurement and the tube leak will be greatly reduced if not eliminated.

Besides the inaccuracy of the measurement, the obtained results show a huge difference in the measured and the simulated results. These differences in the stator core loss clearly indicate the adverse effects of the manufacturing process on the cores of electrical machines. As for the high speed application *i.e.* high frequency application, the effects of manufacturing are more damaging. Previous studies conducted (Section 2.2) on the effects of manufacturing process, address the individual step of the process and show noticeable increase in the core loss. The significant increase observed during this study can be attributed to the compounding adverse effects and material deterioration incurred at each step of the manufacturing process of the stator core.

Segregation of the increased losses to the increase in hysteresis loss and the eddy-current loss is essential for further study of the manufacturing effects. This can be done by preventing the increase in the eddy-current loss due to the manufacturing effects, *i.e.* by deburring the punched laminations and ensuring proper inter-laminar insulation together with some alternate method of clamping (other than welding). These modifications during the core manufacturing will eliminate the inter-laminar short circuit paths and thus limit the increase in the eddy-current loss. Subsequently the measured increase in losses will constitute only the increased hysteresis loss due to manufacturing, which along with the current measured data can yield the increase in the eddy-current loss due to manufacturing.

Conclusion

Finally, from the above discussion and the obtained results, it can be concluded that the constructed measurement setup has higher than acceptable inaccuracy. Partly owing to the poor thermal insulation of the fiber-glass tube, especially at 2.5 mm thickness. Despite the inaccuracy in measurement, the difference in the measured and the simulated (FCSMEK) stator core loss at various supply frequencies and voltage was found to be significant, *i.e.* the measured stator core losses were approximately twice the simulated ones for all the three cores used in the measurement. The significant difference in the measured and the simulated values of the stator core loss suffice the quest of this research. However, for the future purpose to study the effect of the heat treatment on the core losses, the level of inaccuracy in measuring the stator core loss will be unacceptable, especially if the reduction due to the heat treatment is comparable to the measurement errors.

References

[1] J. Pyrhönen, T. Jokinen, and V. Hrabovcova´, *Design of rotating electrical machines*. Chichester: Wiley, 2008.

[2] P. Beckley, *Electrical steels for rotating machines*. IEE power and energy series, Institution of Electrical Engineers, 2002.

[3] T. Nakata, M. Nakano, and K. Kawahara, "Effects of stress due to cutting on magnetic characteristics of silicon steel," *IEEE Translation Journal on Magnetics in Japan*, vol. 7, no. 6, pp. 453 –457, 1992.

[4] A. J. Moses, N. Derebasi, G. Loisos, and A. Schoppa, "Aspects of the cut-edge effect stress on the power loss and flux density distribution in electrical steel sheets," *Journal of Magnetism and Magnetic Materials*, vol. 215-216, pp. 690 – 692, 2000.

[5] W. Arshad, T. Ryckebusch, F. Magnussen, H. Lendenmann, B. Eriksson, J. Soulard, and B. Malmros, "Incorporating lamination processing and component manufacturing in electrical machine design tools," in *Industry Applications Conference, 2007. 42nd IAS Annual Meeting. Conference Record of the 2007 IEEE*, pp. 94 –102, 2007.

[6] F. Ossart, E. Hug, O. Hubert, C. Buvat, and R. Billardon, "Effect of punching on electrical steels: Experimental and numerical coupled analysis," *IEEE Transactions on Magnetics*, vol. 36, pp. 3137 –3140, Sept. 2000.

[7] A. Kedous-Lebouc, B. Cornut, J. C. Perrier, P. ManfÃ©, and T. Chevalier, "Punching influence on magnetic properties of the stator teeth of an induction motor," *Journal of Magnetism and Magnetic Materials*, vol. 254-255, pp. 124 – 126, 2003.

[8] Y. Kurosaki, H. Mogi, H. Fujii, T. Kubota, and M. Shiozaki, "Importance of punching and workability in non-oriented electrical steel sheets," *Journal of Magnetism and Magnetic Materials*, vol. 320, no. 20, pp. 2474 – 2480, 2008. Proceedings of the 18th International Symposium on Soft Magnetic Materials.

[9] P. Baudouin, A. Belhadj, F. Breaban, A. Deffontaine, and Y. Houbaert, "Effects of laser and mechanical cutting modes on the magnetic properties of low and medium si content nonoriented electrical steels," *IEEE Transactions on Magnetics*, vol. 38, pp. 3213 – 3215, Sept. 2002.

[10] A. Arkkio, "Lecture notes of the course S-17.3050 Special Course on Electromechanics P(Modelling of the temperature rise and designing the cooling of electrical machines.), Aalto University, School of Science of Technology." `https://noppa.tkk.fi/noppa/kurssi/s-17.3050/luennot/S-17_3050_lecture_5.pdf`, 2010.

[11] A. Schoppa, J. Schneider, C. D. Wuppermann, and T. Bakon, "Influence of welding and sticking of laminations on the magnetic properties of non-oriented electrical steels," *Journal of Magnetism and Magnetic Materials*, vol. 254-255, pp. 367 – 369, 2003.

[12] C. Kaido, H. Mogi, and K. Hanzawa, "The effect of short circuit between laminated steel sheets on the performance of lamination core of motor," *IEEJ Transactions on Fundamentals and Materials*, vol. 123, no. 9, pp. 857–862, 2003.

[13] S. B. AB, "Non oriented electrical steel." `http://www.sura.se/Sura/hp_main.nsf/startupFrameset?ReadForm`.

[14] C. P. Ltd., "Electrical steel non oriented fully processed." `http://www.cogent-power.com`, 2002.

[15] L. Mthombeni and P. Pillay, "Core losses in motor laminations exposed to high frequency or nonsinusoidal excitation," in *Industry Applications Conference, 2003. 38th IAS Annual Meeting. Conference Record of the*, vol. 2, pp. 1090 – 1097 vol.2, oct. 2003.

[16] M. Takezawa, K. Kitajima, Y. Morimoto, J. Yamasaki, and C. Kaido, "Effect of strain by mechanical punching on nonoriented si-fe electrical sheets for a nine-slot motor core," *IEEE Transactions on Magnetics*, vol. 42, pp. 2790 –2792, oct. 2006.

[17] A. Moses and H. Rahmatizadeh, "Effects of stress on iron loss and flux distribution of an induction motor stator core," *IEEE Transactions on Magnetics*, vol. 25, pp. 4003 –4005, Sept. 1989.

[18] A. Bousbaine, W. F. Low, and M. McCormick, "Novel approach to the measurement of iron and stray load losses in induction motors," *IEE Proceedings - Electric Power Applications*, vol. 143, no. 1, pp. 78–86, 1996. ID: 1.

[19] A. J. Gilbert, "A method of measuring loss distribution in electrical machines," *Proceedings of the IEE - Part A: Power Engineering*, vol. 108, no. 39, pp. 239–244, 1961. ID: 1.

[20] Y. Guo, J. G. Zhu, J. Zhong, H. Lu, and J. X. Jin, "Measurement and modeling of rotational core losses of soft magnetic materials used in electrical machines: A review," *IEEE Transactions on Magnetics*, vol. 44, no. 2, pp. 279–291, 2008. ID: 1.

[21] M. D. Wulf, L. Dupre, D. Makaveev, and J. Melkebeek, "Needle-probe techniques for local magnetic flux measurements," *Journal of Applied Physics*, vol. 93, no. 10, pp. 8271–8273, 2003. ID: 1.

[22] G. Loisos and A. J. Moses, "Critical evaluation and limitations of localized flux density measurements in electrical steels," *IEEE Transactions on Magnetics*, vol. 37, no. 4, pp. 2755–2757, 2001. ID: 1.

[23] A. A. E. Abdallh, P. Sergeant, G. Crevecoeur, L. Vandenbossche, L. Dupre, and M. Sablik, "Magnetic material identification in geometries with non-uniform electromagnetic fields using global and local magnetic measurements," *IEEE Transactions on Magnetics*, vol. 45, no. 10, pp. 4157–4160, 2009. ID: 1.

[24] G. Crevecoeur, L. Dupre, L. Vandenbossche, and R. V. de Walle, "Reconstruction of local magnetic properties of steel sheets by needle probe methods using space mapping techniques," *Journal of Applied Physics*, vol. 99, no. 8, pp. 08H905–08H905–3, 2006. ID: 1.

[25] S. Tumanski, "Induction coil sensors-a review," *Measurement Science and Technology*, vol. 18, no. 3, p. R31, 2007.

[26] M. Enokizono, M. Morikawa, K. Kawamura, and J. Sievert, "Distribution of two-dimensional magnetic properties in three-phase induction motor model core," *IEEE Transactions on Magnetics*, vol. 32, no. 5, pp. 4989–4991, 1996. ID: 1.

[27] D. R. Turner, K. J. Binns, B. N. Shamsadeen, and D. F. Warne, "Accurate measurement of induction motor losses using balance calorimeter," *IEE Proceedings B Electric Power Applications*, vol. 138, no. 5, pp. 233–242, 1991. ID: 1.

A Air Properties

Accurate determination of c_p (specific heat capacity at constant pressure) of the coolant air is essential for the direct measurement type open calorimeter. The coolant air flow is assumed to be incompressible, which implies that c_p of the coolant air depends on Temperature (T_{in}), Atmospheric Pressure (p_0) and Relative Humidity (χ_{rh}) of the inlet air

$$c_p(x) = \frac{c_{p,\text{a}}(T) + x c_{p,\text{w}}(T)}{1+x} \tag{A.1}$$

where, $c_{p,\text{a}}(T)$ and $c_{p,\text{w}}(T)$ are the specific heat capacity of dry air and water vapor respectively, and x is the specific humidity. The average values of $c_{p,\text{a}}$ and $c_{p,\text{w}}$ within the range of operation, *i.e.* $T \in [20,\, 80]\,^0C$, are accurate enough to be used in equation (A.1). However, determining the specific humidity requires measurement of the atmospheric pressure and the relative humidity along with the air temperature, at the inlet of the calorimeter.

$$x = \frac{\rho_{\text{w}}}{\rho_{\text{a}}} \tag{A.2}$$

where, ρ_{w} and ρ_{a} are the density of dry air and water vapor respectively, at the inlet temperature. ρ_{w} and ρ_{a} can be calculated as:

$$\begin{aligned} \rho_{\text{w}} &= \frac{p_{\text{w}}}{R_{\text{w}} T_{\text{in}}} \\ \rho_{\text{a}} &= \frac{p_{\text{a}}}{R_{\text{a}} T_{\text{in}}} = \frac{p_0 - p_{\text{w}}}{R_{\text{a}} T_{\text{in}}} \end{aligned} \tag{A.3}$$

where, p_{a} and p_{w} are the partial pressures of dry air and water vapor respectively. R_{a} and R_{w} are the gas constants of dry air and water vapor respectively. p_{w} is a function of the relative humidity(χ_{rh}) and the saturation vapor pressure(p_{ws}).

$$p_{\text{w}} = \chi_{\text{rh}} \times p_{\text{ws}}\left(T_{\text{in}}\right) \tag{A.4}$$

The saturation vapor pressure can be estimated as:

$$p_{\text{ws}}\left(T_{\text{in}}\right) = \frac{e^{77.345 + 0.0057(T_{\text{in}}) - \frac{7235}{T_{\text{in}}}}}{\left(T_{\text{in}}\right)^{8.2}} \tag{A.5}$$

where, T_{in} is the inlet air temperature in Kelvin and p_{ws} is in Pascal.

B Flow Nozzle

A flow nozzle is used to measure the volumetric flow rate of a fluid. It is identical to the venture meter and works on the same principle, *i.e.* Bernoulli's Principle.

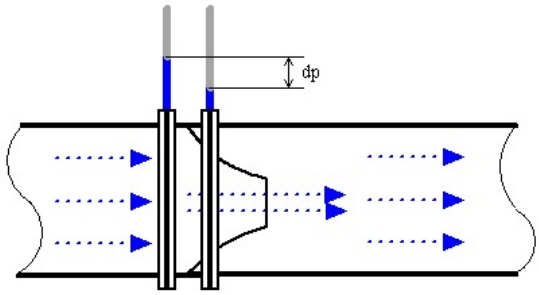

Figure B.1: *Flow Nozzle*

Assuming the fluid flow to be incompressible and laminar in a horizontal pipe, and neglecting the friction losses, Bernoulli's equation at steady state reduces to

$$p_1 + \frac{1}{2}\rho V_1^2 = p_2 + \frac{1}{2}\rho V_2^2$$

$$p_1 - p_2 = \frac{1}{2}\rho V_1^2 - \frac{1}{2}\rho V_2^2 \tag{B.1}$$

where, p_1 and p_2 are the upstream and downstream pressures respectively, V_1 and V_2 are the upstream velocity and the orifice outlet velocity of the fluid respectively. ρ is the density of the fluid. Using the continuity equation ($Q_\mathrm{v} = A_1V_1 = A_2V_2$), equation (B.1) becomes

$$p_1 - p_2 = \frac{1}{2}\rho\left(\frac{Q_\mathrm{v}}{A_1}\right)^2 - \frac{1}{2}\left(\frac{Q_\mathrm{v}}{A_2}\right)^2 \tag{B.2}$$

where, Q_v is the volumetric flow rate of the fluid, A_1 and A_2 are cross sectional areas of the inlet pipe and the orifice hole respectively. Solving for Q_v we get,

$$Q_\mathrm{v} = A_2\sqrt{\frac{2\left(p_1 - p_2\right)/\rho}{1 - \left(A_2/A_1\right)^2}}$$

$$Q_\mathrm{v} = A_2\frac{1}{\sqrt{1 + \left(D_2/D_1\right)^4}}\sqrt{2\left(p_1 - p_2\right)/\rho} \tag{B.3}$$

where, D_1 and D_2 are the pipe diameter and the orifice hole diameter respectively. The above equations are for an ideal case. The friction losses, viscosity and turbulence effects are compensated by introducing a factor called coefficient of discharge

C_d which depends on the Reynolds number (Re) and beta factor ($i.e.\,\beta = D_2/D_1$). Furthermore, the effect of compressibility, normally for gaseous fluid, is dealt by introducing another factor called the expansion factor ε. Finally the volumetric flow rate and the mass flow rate (including all the above mentioned factors) are given by

$$Q_\mathrm{v} = \varepsilon C_\mathrm{d} A_2 \frac{1}{\sqrt{1+\beta^4}} \sqrt{2\left(p_1 - p_2\right)/\rho} \tag{B.4}$$

$$Q_\mathrm{m} = \rho Q_\mathrm{v} = \varepsilon C_\mathrm{d} A_2 \frac{1}{\sqrt{1+\beta^4}} \sqrt{2\rho\left(p_1 - p_2\right)} \tag{B.5}$$

The expansion factor and the coefficient of discharge (ISO 1932) can be calculated as

$$\varepsilon = 1 - \left(0.41 + 0.35\,\beta^4\right) \frac{p_1 - p_2}{\chi p_1} \tag{B.6}$$

$$C_\mathrm{d} = 0.9965 - 0.00653 \left(\frac{10^6 \beta}{Re}\right)^{0.5} \tag{B.7}$$

Valid for:

$$0.2 \leq \beta \leq 0.8,\ 10^4 \leq Re \leq 10^7 \text{ and } 50\,\mathrm{mm} \leq D \leq 630\,\mathrm{mm}$$

$$C_\mathrm{d} = 0.99 - 0.2262\beta^{4.1} - \left(0.00175\beta^2 - 0.0033\beta^{4.15}\right) \left(\frac{10^6}{Re}\right)^{1.15} \tag{B.8}$$

Valid for:

$$\begin{aligned} &50\,\mathrm{mm} \leq D \leq 500\,\mathrm{mm} \\ \text{and } &0.3 \leq \beta \leq 0.44;\ 7 \times 10^4 \leq Re \leq 10^7 \\ \text{or } &0.44 \leq \beta \leq 0.8;\ 2 \times 10^4 \leq Re \leq 10^7 \end{aligned}$$

The Reynolds Number and χ (Isentropic coefficient) can be calculated as

$$Re = \frac{\rho V_1 D_1}{\mu} \tag{B.9}$$

$$\chi = \frac{c_p}{c_p - R_\mathrm{a}} \tag{B.10}$$

where, μ and R_a are the dynamic viscosity and the gas constant of air respectively.

C Computation of Uncertainty

Root Sum Squared

There are two methods to compute uncertainty, both based on the Root Sum Squared (RSS) estimate of the errors.

i Analytical Method

ii Sequential Perturbation

Let's assume,

$$R = f(x_1, x_2, \cdots, x_n)$$

where R is the final calculated result, and x_i are measured quantities. Let u_i be the uncertainty in the measured value of x_i (*i.e.* $x_i = x_{\text{measured},i} \pm u_i$). From the basic definition of RSS estimate, the uncertainty in R due to the error in each x_i is:

$$u_R = \left[\left(\frac{\partial R}{\partial x_1} u_1 \right)^2 + \left(\frac{\partial R}{\partial x_2} u_2 \right)^2 + \cdots + \left(\frac{\partial R}{\partial x_n} u_n \right)^2 \right]^{1/2} \tag{C.1}$$

In the analytical method, a single formula for the uncertainty in a measurement is derived. This makes the computation of the uncertainty straightforward and rapid. However, deriving the formula is cumbersome and any change in the measurement chain requires re-deriving of the formula. The analytical method eventually becomes impractical as R becomes increasingly complex. From the fundamental theorem of calculus, partial derivative of a function is:

$$\frac{\partial R}{\partial x_1} = \lim_{\Delta x_i \to 0} \left[\frac{R(x_i + \Delta x_i) - R(x_i)}{\Delta x_i} \right] \approx \frac{R(x_i + \delta x_i) - R(x_i)}{\delta x_i} \tag{C.2}$$

where, δx_i is a finite perturbation in the measured value of x_i. Assuming $\delta x_i \approx u_i$, we get,

$$\left[\frac{\partial R}{\partial x_1} u_1 \right]^2 \approx \left[\frac{R(x_i + \delta x_i) - R(x_i)}{\delta x_i} u_i \right]^2 \approx \left[R(x_i + \delta x_i) - R(x_i) \right]^2 \tag{C.3}$$

Finally, using equation (C.3) the uncertainty can be computed by sequential perturbation as:

$$u_R = \left[{\Delta R_1}^2 + {\Delta R_2}^2 + \cdots + {\Delta R_n}^2 \right]^{1/2} \tag{C.4}$$

where,

$$\begin{aligned}
\Delta R_1 &= R(x_1 + u_1, x_2, \cdots, x_n) - R(x_1, x_2, \cdots, x_n) \\
\Delta R_2 &= R(x_1, x_2 + u_2, \cdots, x_n) - R(x_1, x_2, \cdots, x_n) \\
&\vdots \\
\Delta R_n &= R(x_1, x_2, \cdots, x_n + u_n) - R(x_1, x_2, \cdots, x_n)
\end{aligned}$$

Equation (C.4) is valid for small perturbations u_i, *i.e.* if any of u_i are large, equation (C.4) might not be a good approximation of equation (C.1). Also, if $R(x_1, x_2, \cdots, x_n)$ is strongly nonlinear, equation (C.4) might not be valid.

Combining Uncertainty

Uncertainty in a primary measured value, when the error sources are random errors, instrumentation errors and calibration errors (assuming that the individual error contributions are uncorrelated), can be estimated as:

$$u_x = \sqrt{u_{x_{\text{rand}}}^2 + u_{x_{\text{inst}}}^2 + u_{x_{\text{cal}}}^2} \tag{C.5}$$

where,
$u_{x_{\text{rand}}}$ is the random errors in measuring x, which can be minimized by averaging a number of readings.
$u_{x_{\text{inst}}}$ is the instrumentation errors, primarily due to the resolution of the measuring instruments.
$u_{x_{\text{cal}}}$ is the calibration errors, specified by the standards or the manufacturers of the sensors.

Propagated Errors

The formulae for the propagated errors in the derived quantity (z) due to the errors in the measured fundamental quantities (x and y) is shown in Table C.1

Table C.1: *Propagated Error*

Function	Propagated Error
$z = ax \pm b$	$\Delta z = a\Delta x$
$z = x \pm y$	$\Delta z = \left((\Delta x)^2 + (\Delta y)^2\right)^{1/2}$
$z = cxy$	$\frac{\Delta z}{z} = \left(\left(\frac{\Delta x}{x}\right)^2 + \left(\frac{\Delta y}{y}\right)^2\right)^{1/2}$
$z = c\frac{x}{y}$	$\frac{\Delta z}{z} = \left(\left(\frac{\Delta x}{x}\right)^2 + \left(\frac{\Delta y}{y}\right)^2\right)^{1/2}$
$z = cx^a$	$\frac{\Delta z}{z} = a\frac{\Delta x}{x}$
$z = cx^a y^b$	$\frac{\Delta z}{z} = \left(\left(a\frac{\Delta x}{x}\right)^2 + \left(b\frac{\Delta y}{y}\right)^2\right)^{1/2}$

D Measured Results

Table D.1: *Measured Core-Losses at* $\hat{B}_{\text{air-gap}} = 0.4\,\text{T}$

$\hat{B}_{\textbf{air-gap}}$	**0.4 T**											
Frequency	Core 1				Core 2				Core 3			
(Hz)	P_{calib} (W)	$P_{\text{tube leak}}$ (W)	P_{stator} (W)	Error (%)	P_{calib} (W)	$P_{\text{tube leak}}$ (W)	P_{stator} (W)	Error (%)	P_{calib} (W)	$P_{\text{tube leak}}$ (W)	P_{stator} (W)	Error (%)
1000	1501±34	238±78	1739±112	6.4	1417±36	304±96	1721±131	7.6	1566±37	207±70	1773±107	6.0
900	1297±19	185±61	1482±80	5.4	1235±35	239±78	1473±113	7.7	1357±33	156±53	1513±86	5.7
800	1128±19	144±50	1272±69	5.4	1033±32	169±57	1203±89	7.4	1164±31	126±45	1290±76	5.9
700	953±25	120±41	1073±67	6.2	866±28	134±49	1000±77	7.7	968±26	100±37	1068±63	5.9
600	776±25	131±44	908±69	7.6	710±21	135±45	845±65	7.7	756±27	95±35	851±62	7.3
500	582±15	87±31	669±46	6.9	533±18	145±47	677±66	9.7	619±24	62±25	680±49	7.2
400	402±12	115±38	554±50	9.0	385±15	83±30	468±46	9.7	429±29	97±34	526±63	11.9
300	276±11	80±29	356±40	11.3	274±13	0±0	274±13	4.7	302±21	60±25	362±46	12.7

Table D.2: *Measured Core-Losses at* $\hat{B}_{\text{air-gap}} = 0.35\,\text{T}$

$\hat{B}_{\textbf{air-gap}}$	**0.35 T**											
Frequency	Core 1				Core 2				Core 3			
(Hz)	P_{calib} (W)	$P_{\text{tube leak}}$ (W)	P_{stator} (W)	Error (%)	P_{calib} (W)	$P_{\text{tube leak}}$ (W)	P_{stator} (W)	Error (%)	P_{calib} (W)	$P_{\text{tube leak}}$ (W)	P_{stator} (W)	Error (%)
1000	1284±34	160±54	1444±88	6.1	1154±32	254±82	1407±115	8.1	1273±34	165±55	1437±89	6.2
900	1107±30	136±48	1243±79	6.3	990±29	186±61	1175±90	7.7	1097±29	140±49	1237±78	6.3
800	947±28	105±38	1051±65	6.2	836±27	147±53	983±79	8.1	936±27	116±40	1052±68	6.4
700	792±25	84±33	875±58	6.6	708±26	114±40	821±65	8.0	777±23	92±35	870±58	6.6
600					565±18	120±41	684±59	8.7				

Table D.3: *Measured Core-Losses at* $\hat{B}_{\text{air-gap}} = 0.3\,\text{T}$

$\hat{B}_{\textbf{air-gap}}$	**0.3 T**											
Frequency	Core 1				Core 2				Core 3			
(Hz)	P_{calib} (W)	$P_{\text{tube leak}}$ (W)	P_{stator} (W)	Error (%)	P_{calib} (W)	$P_{\text{tube leak}}$ (W)	P_{stator} (W)	Error (%)	P_{calib} (W)	$P_{\text{tube leak}}$ (W)	P_{stator} (W)	Error (%)
1000	996±20	110±43	1106±63	5.7	899±25	187±62	1086±87	8.0	978±32	117±44	1095±77	7.0
900	863±20	87±34	950±53	5.6	773±25	152±49	926±74	8.0	849±24	97±36	947±60	6.3
800	735±20	57±24	792±44	5.5	644±25	119±41	763±66	8.7	714±23	68±27	781±50	6.4
700	606±18	43±21	649±39	6.0	547±23	78±29	625±52	8.3	606±21	55±24	661±45	6.8
600					412±15	106±36	518±51	9.8				